ADVANCING EARTH AND SPACE SCIENCES

JGR Atmospheres

RESEARCH ARTICLE

10.1029/2025JD043846

Key Points:

- Hydrodynamic-ice modeling of Lake Nam Co reveals space-time variations in thermo-hydrodynamics and underlying mechanisms
- Lateral heat transport and freeze-thaw processes are main factors determining the horizontal thermal variability
- Mid-lake gyre is primarily cyclonic during winter, but varies interannually during summer-autumn due to the over-lake mesoscale wind structure

Correspondence to:

A. Huang,
anhuang@nju.edu.cn

Citation:

Wu, Y., Huang, A., Lu, Y., & Fujisaki-Manome, A. (2025). Application of a three-dimensional coupled hydrodynamic-ice model for a large and deep dimictic lake over Tibetan Plateau: Thermo-hydrodynamic variations during 2007–2017. *Journal of Geophysical Research: Atmospheres*, *130*, e2025JD043846. https://doi.org/10.1029/2025JD043846

Received 11 MAR 2025
Accepted 9 JUN 2025

Author Contributions:

Conceptualization: Anning Huang
Data curation: Yang Wu, Ayumi Fujisaki-Manome
Formal analysis: Yang Wu, Youyu Lu, Ayumi Fujisaki-Manome
Investigation: Yang Wu, Anning Huang, Youyu Lu, Ayumi Fujisaki-Manome
Methodology: Yang Wu
Resources: Yang Wu, Youyu Lu, Ayumi Fujisaki-Manome
Software: Yang Wu
Supervision: Anning Huang
Validation: Yang Wu, Anning Huang, Youyu Lu
Visualization: Yang Wu
Writing – original draft: Yang Wu, Anning Huang, Youyu Lu, Ayumi Fujisaki-Manome
Writing – review & editing: Yang Wu, Anning Huang, Youyu Lu, Ayumi Fujisaki-Manome

Application of a Three-Dimensional Coupled Hydrodynamic-Ice Model for a Large and Deep Dimictic Lake Over Tibetan Plateau: Thermo-Hydrodynamic Variations During 2007–2017

Yang Wu[1,2], **Anning Huang**[3], **Youyu Lu**[4], and **Ayumi Fujisaki-Manome**[5]

[1]Nanjing Innovation Institute for Atmospheric Sciences, Chinese Academy of Meteorological Sciences–Jiangsu Meteorological Service, Nanjing, China, [2]Jiangsu Key Laboratory of Severe Storm Disaster Risk, Key Laboratory of Transportation Meteorology of CMA, Nanjing, China, [3]School of Atmospheric Sciences, Nanjing University, Nanjing, China, [4]Fisheries and Oceans Canada, Bedford Institute of Oceanography, Dartmouth, NS, Canada, [5]Cooperative Institute for Great Lakes Research, University of Michigan, Ann Arbor, MI, USA

Abstract The space-time variations of thermo-hydrodynamics and underlying mechanisms in Lake Nam Co, the third largest lake over Tibetan Plateau, are investigated using the simulations from a three-dimensional lake-ice coupled model during 2007–2017. The model well reproduces the seasonal lake thermodynamics, highlighting the phases of summer-autumn warm thermal stratification, late-autumn overturning, winter-spring inverse thermal stratification, and late-spring overturning. Heat budget analysis underscores the importance of lateral heat transport and ice freeze-thaw processes in shaping the horizontal thermal variability. During 2007–2017, lake surface temperature, as well as the duration, onset and end of warm thermal stratification, show significant interannual variations related to the surface air temperature and ice conditions. During winter-spring, the lake water flow speed shows strong interannual variability related to wind speed and ice conditions. Nevertheless, a consistent circulation pattern is found, featuring a dominant mid-lake cyclonic gyre, upwelling along the western coast, and strong coastal currents driven by the prevailing southwesterly winds during December–January, followed by weakened lake water motions during February–April when the packed ice inhibits the wind stress input. In contrast, the summer-autumn lake circulation is weaker but more variable, with the mid-lake circulation shifting between being cyclonic (caused by the combined effects of southwesterly winds, positive wind stress curl and density effects) and occasionally anti-cyclonic (due to the presence of negative wind stress curl).

Plain Language Summary Reliable information on lake thermal structure and circulation is essential for interdisciplinary researches such as transport of biological and chemical tracers, water quality prediction and ecosystem management. In this study, we use a three-dimensional lake-ice coupled model to investigate the space-time variations of thermo-hydrodynamics and underlying mechanisms in Lake Nam Co, the third largest lake over Tibetan Plateau. The results reveal the dimictic features of seasonal lake thermodynamics, pointing out the significant role of lateral heat transport and ice freeze-thaw processes in driving the horizontal thermal variability. During 2007–2017, the lake surface temperature and the duration, onset and end of warm thermal stratification show considerable interannual variability as a response to the surface air temperature and ice conditions. The lake circulation pattern is coherent during winter due to the prevailing southwesterly wind, and shows significant interannual variations during summer-autumn due to the variable over-lake mesoscale wind structure.

1. Introduction

The Tibetan Plateau (TP), known as the "Earth's Third Pole" and "Water Tower of Asia" (Qiu, 2008), hosts the highest alpine lake concentration in the world (Zhang, Chen, et al., 2020). Owing to the intense solar forcing during summer and low air temperature during winter, the thermal regime of most high-altitude lakes is dimictic (Kirillin et al., 2017), featured by long-lasting stratified and ice-covered phases, each for 4–5 months. The seasonal evolutions of lake thermal stratification and ice significantly impact the distribution and exchange of nutrients, oxygen and carbon within lakes, and thus a wide range of physical and biogeochemical processes (Holland & Kay, 2003; Kraemaer et al., 2021; Maberly et al., 2020). Moreover, the space-time variations of lake surface temperature and ice conditions play a vital role in determining the timing, intensity and location of lake-effect weather, mainly via influencing the moisture, heat and momentum fluxes between water and atmosphere (Fujisaki et al., 2017; Qi & Xue, 2019; Wright et al., 2013). The lake circulation and ice drift further add complexity to the spatial variability of large-lake thermodynamics and related climatic effect (Sun et al., 2014; Xue et al., 2017). Addressing the space-time variations of thermo-hydrodynamics and the underlying mechanisms is important for understanding the large seasonally ice-covered TP lakes due to the ecological, biogeochemical and climatological relevance.

During recent years, a number of studies incorporating field measurements and satellite remote sensing have been promoted to investigate the lake thermodynamics and water-ice-atmosphere interactions over TP (Gou et al., 2017; Qu et al., 2012; Wang, 2020; Wang et al., 2015). The in situ observed water temperature profiles show that warm thermal stratification forms and persists from early June to early November in several large TP lakes, for example, Lake Nam Co (LNC; Wang et al., 2020), Lake Mapam Yumco and La'ang Co (Su et al., 2021; Wang et al., 2013), and Lake Dagze Co and Bangong Co (Wang et al., 2014; Xiao et al., 2015). The basin size, water depth and transparency can lead to evident spatial variations of lake thermodynamics in LNC (Wang et al., 2019). The TP lakes start to freeze up in late October, become fully ice-covered in mid-January of the following year, start to break up ice in late March, and become ice-free in early July (Cai et al., 2019). During the ice-covered phase, a stable inverse thermal stratification forms, with the under-ice lake surface temperature typically falling below the temperature of maximum water density (T_{dmax}, Huang et al., 2021). In the melting phase, the intensified solar radiation could easily penetrate the highly transparent ice, heating the upper water volume toward T_{dmax}. This process triggers density-driven convection until the under-ice lake surface temperature reaches T_{dmax}, after which it rapidly rises to form a warm thermal stratification before ice break-up (Lazhu et al., 2020). Subsurface water temperature can go up to 6–8°C and the resulting strong ice-water fluxes make a crucial contribution to ice ablation (Huang et al., 2019; Kirillin et al., 2021). For large dimictic lakes, the thermodynamics has been reported to show evident seasonal/interannual evolution and spatial variability due to the lake-air heat exchange and wind/density-driven circulations (Boyce et al., 1989; Mortimer, 1987). However, in situ measurements are still scant due to the remoteness of TP, and satellite-derived images are confined to lake surface conditions and limited by inadequate space-time resolution and cloud contamination (Guo et al., 2018). Analyses using in situ and satellite data are inadequate to address the space-time variations of thermo-hydrodynamics and their underlying causes.

Three-dimensional (3-D) hydrodynamic models serve as effective tools to advance understanding the thermo-hydrodynamic processes within large dimictic lakes. For example, fragmentary observations from the Laurentian Great Lakes indicate that during the stratified phase, lake surface temperature shows a nearshore-offshore gradient, the thermocline features a dome shape, and the mean circulation is typically cyclonic (Beletsky et al., 1999; Harrington, 1895; McCULLOCH, 1973; Pickett & Richards, 1975). Several mechanisms, for example, the asymmetric response of surface stress to a uniform wind (Emery & Csanady, 1973), heat transport divergence (Csanady, 1977), Lagrange drift induced by internal Kelvin waves (Wunsch, 1973), and Ekman transport/pumping effects of cyclonic surface winds (Gill, 1982), have been proposed to explain the dome-shaped thermocline and cyclonic flow. Despite these insights, the intricacies of lake thermo-hydrodynamics, particularly regarding the climatological state, seasonal/interannual variability and the relative importance of driving factors, remain uncertain due to the scarcity of comprehensive lake-wide observations. Long-term simulations of 3-D thermal structure and circulations could bridge the knowledge gaps (Bai et al., 2013; Bennington et al., 2010; Schwab et al., 1995). Based on hydrodynamic simulations under various forcing scenarios, Schwab and Beletsky (2003) concluded that baroclinicity played a more (less) crucial role than the positive wind stress curl in determining the predominantly cyclonic flow in Lake Michigan during summer (winter). During the ice-covered phase, lake ice, which shows strong sensitivity and space-time variability in response to atmospheric forcings (Wang et al., 2012), is identified to substantially alter the lake thermal structure and hydrodynamic processes via modulation of lake-air interactions (Austin & Colman, 2007; Bai et al., 2020). Lower ice coverage allows the water body to receive more net wind stress from the surface atmosphere (Fujisaki et al., 2013), resulting in more energetic nearshore waves and currents. Furthermore, a shortened ice duration corresponds to an extended phase of spring radiative heating, which favors an earlier and warmer summer thermal stratification (Woolway et al., 2020), and in turn influences lake circulation patterns.

Among the great number of seasonally ice-covered lakes in TP, 13 lakes have areas exceeding 500 km^2 and 3 lakes over 2,000 km^2 (Lu et al., 2019), namely Lake Qinghai (~4,400 km^2, China's largest lake), Lake Siling Co

(~2,349 km^2), and LNC (~2,028 km^2). The thermo-hydrodynamics of these large lakes are not only influenced by the local lake-air turbulent exchanges and vertical mixing within the water column, but are also regulated by wind-driven processes and temperature-flow interactions. Observations have revealed pronounced spatiotemporal variability in their freeze-thaw processes (Gou et al., 2017; Qi et al., 2019, 2020) and lake surface temperature (Ke & Song, 2014; Xiao et al., 2013). Presently, one-dimensional (1-D) lake models are still widely used for numerical studies of large seasonally ice-covered TP lakes, while the evident deficiencies of 1-D models have been recognized (Bennington et al., 2014; Wu et al., 2020; Xue et al., 2017). Such deficiencies hinder comprehensive understanding of lake thermodynamics and hydrodynamic processes including ice drift, water level fluctuations, and circulation patterns. When 1-D models are implemented in coupled modeling systems, these limitations may compromise the representation of lake-air interactions and consequently reduce the predictive capability for lake-effect weather systems. Taking LNC as an example, previous in situ and satellite-based studies have identified distinct east-west asymmetries in its freeze-thaw processes, characterized by earlier freezing and later melting in eastern basins compared to western basins (Gou et al., 2017; Qu et al., 2012). This spatial asymmetry, caused by the prevailing winter-spring westerlies and associated ice-current dynamics, cannot be realistically simulated by 1-D lake models. Thus, a 3-D lake-ice coupled model (ICEPOM) was applied to obtain simulated ice cover/thickness, surface water temperature and lake thermal structure that are consistent with observational data, and to understand the dynamic causes of the space-time variations of ice (Wu et al., 2023). In this study, we extend the analysis to address two remaining questions, that is, (a) how does ice presence modulate lake thermo-hydrodynamics? And (b), is there interannual variability of lake circulation during the ice-free phase and what are the causes? Answering these questions will advance understanding the impacts of large seasonally ice-covered TP lakes on regional climate and improving the representation of these lakes in coupled models.

2. ICEPOM Model Description

ICEPOM integrates the hydrodynamic model Princeton Ocean Model (POM; Blumberg & Mellor, 1987) with a two-dimensional ice dynamic model based on the elastic-viscous-plastic rheology (Hibler, 1979, 1980; Hunke & Dukowicz, 1997) and a 0-layer ice thermodynamic model (Parkinson & Washington, 1979; Semtner, 1976). The model configuration employs 1-km horizontal grids and 31 terrain-following sigma vertical layers, with enhanced resolution near the surface and bottom boundaries (Wang et al., 2009). The hydrodynamic component incorporates the Mellor-Yamada level 2.5 turbulence closure scheme (Mellor & Yamada, 1982), Smagorinsky horizontal diffusion scheme (Smagorinsky, 1963), Coupled Ocean-Atmosphere Response Experiment Met Flux Algorithm version 3.0 (Fairall et al., 1996, 2003), quadratic bottom drag coefficient, and zero heat and volume fluxes across the coastal and bottom boundaries (Beletsky et al., 2013; Fujisaki et al., 2012). For ice modeling, we adopt the standard parameterizations of Parkinson and Washington (1979) with modifications from Fujisaki et al. (2012). A temperature-dependent surface ice albedo scheme (Subin et al., 2012) is used, and the maximum and minimum ice albedo values are set to 0.5 and 0.1, respectively, based on observations (Lang et al., 2018). The model uses time steps of 1 s (external mode) and 60 s (internal mode) for hydrodynamics, and 20 s (dynamics) and 60 s (thermodynamics) for ice processes.

ICEPOM is forced by surface wind stress and heat flux, calculated using data from the China Meteorological Forcing Data (CMFD, https://data.tpdc.ac.cn/en/, He et al., 2020), including surface downward shortwave and longwave radiation, surface air pressure, 2-m air temperature, 2-m relative humidity, and 10-m wind speed. The CMFD has a horizontal resolution of 0.1° × 0.1° in latitude/longitude, and 3-hourly in time. Following Hsu (1988), an empirical formula $Y = 1.17X + 1.62$ is applied to adjust the original underestimated wind speed of CMFD (denoted as X) to the realistic value (denoted as Y). The wind direction, which is not provided by CMFD, is interpolated from the ERA5-Land reanalysis data set (https://cds.climate.copernicus.eu; Muñoz-Sabater, 2019). The realism of the forcing data was evaluated against in situ observations in Wu et al. (2023).

ICEPOM simulations span from 20th May 1999 to 31st December 2017, initialized with zero currents, zero ice cover, a salinity of 1.7 g·L^{-1}, and homogeneous water temperature of 2.52°C. Simulations from 1999 to 2006 are taken as the spin-up phase, and the results during 2007–2017 are used for a comprehensive analysis of lake thermal structure and circulation on seasonal to interannual time scales. More detailed model configurations and experimental designs are documented in our previous work (Wu et al., 2023).

3. Analysis Methodology

At each grid point i, the effective ice thickness (AH_i) is defined as the product of ice concentration (A_i) and ice thickness (H_i). The ice volume is then calculated by multiplying AH_i with the area of grid cell. The lake surface temperature (LST) is calculated as the sum of ice surface temperature and water surface temperature (LSWT) weighted by A_i and $(1 - A_i)$, respectively. The ice-on (ice-off) date is determined as the first (last) date when AH_i is above (below) 0.01 m, and the ice duration is the total number of days between them. The onset (end) date of warm thermal stratification is defined as the first (last) date when the temperature difference between surface and bottom waters exceeds 1°C, with the duration being the total number of days between them. Autumnal overturning denotes the transition phase that separates the stratified phases of summer and winter, characterized by strong mixing in the vertical. Hence, the onset of autumnal overturning is defined the same as the end of summer thermal stratification. The end of autumnal overturning coincides with the onset of winter inverse stratification, defined as the first date when LSWT drops to $\mathrm{T}_{\mathrm{dmax}}$. Note that $\mathrm{T}_{\mathrm{dmax}}$ depends on the surface air pressure and water salinity (Chen & Millero, 1986). It is typically 4°C for freshwater, and is lower for alpine saline lakes, for example, estimated to be ~3.60°C with a surface air pressure of 0.57 bar and a salinity of 1.7 g/L for LNC (Wang et al., 2019). Moreover, we define winter as December to the following February, spring as March to May, summer as June to August, and autumn as September to November.

The heat balance for a lake water column is formulated as follows (Titze & Austin, 2014; Wetzel & Likens, 2000):

$$\frac{\delta}{\delta t}\mathrm{LHC} = \mathrm{SNHF}_{\downarrow} + \theta_{\mathrm{hor}} + \theta_{\mathrm{sed}} \tag{1}$$

$$\mathrm{LHC} = C_{\mathrm{pw}} \int_0^h \rho_w(z)\, T_w(z)\, dz \tag{2}$$

$$\begin{aligned} \mathrm{SNHF}_{\downarrow} = {} & \mathrm{SW}_{\downarrow} + \mathrm{LW}_{\downarrow} - \mathrm{LW}_{\uparrow} - \mathrm{SH}_{\uparrow} - \mathrm{LH}_{\uparrow} \\ & - fb_{\uparrow} + \mathrm{hflx}_{\mathrm{imf}\downarrow} \end{aligned} \tag{3}$$

where LHC is the lake heat content within the water column, and its time derivative, $\delta\mathrm{LHC}/\delta\mathrm{t}$ (in W m^{-2}), is balanced by the surface net heat flux ($\mathrm{SNHF}_{\downarrow}$), the convergence of depth-integrated horizontal heat transport due to advection and diffusion (θ_{hor}), and the conductive heat exchange between water and bottom sediments (θ_{sed}). In Equation 2, $C_{\mathrm{pw}} = 4,180\ \mathrm{J\ kg^{-1}\ K^{-1}}$ is the specific heat of water, h is the lake depth (in m), $\rho_w(z)$ (in kg m^{-3}) and $T(z)$ (in °C) are the water density and temperature at depth z (in m), respectively. In Equation 3, $\mathrm{SNHF}_{\downarrow}$ is the sum of surface downward shortwave ($\mathrm{SW}_{\downarrow}$) and longwave ($\mathrm{LW}_{\downarrow}$) radiation, upward longwave radiation ($\mathrm{LW}_{\uparrow}$), upward sensible ($\mathrm{SH}_{\uparrow}$) and latent ($\mathrm{LH}_{\uparrow}$) heat, upward ice-water heat flux ($fb_{\uparrow}$), and downward heat due to ice formation/ablation ($\mathrm{hflx}_{\mathrm{imf}\downarrow}$). Due to the use of adiabatic bottom boundary conditions ($\theta_{\mathrm{sed}} = 0$), $\theta_{\mathrm{hor}} = \delta\mathrm{LHC}/\delta t - (\mathrm{LHC} + \mathrm{SNHF}_{\downarrow})$. Positive values of $\mathrm{SNHF}_{\downarrow}$ and θ_{hor} indicate that the local lake column is gaining heat. These heat budget components were first calculated based on the daily ICEPOM output and then averaged over bimonthly intervals for analysis.

4. Seasonal Variations

4.1. LST, LSWT, and Lake Column Heat Balance

Figure 1 shows the bimonthly LST/LSWT, ice, and surface currents in the top 3 m based on the ICEPOM simulations averaged over 2007–2017. From June to November, LNC is in its ice-free phase, and the modeled LST matches LSWT precisely. During this phase, winds predominantly originate from the south-southwest, leading to noticeable horizontal variability of LST and currents. In June–July, LST features a nearshore-offshore gradient, and the surface currents form a cyclonic gyre in the main basin and an anti-cyclonic gyre in the smaller eastern basin (Figure 1a). In August–September, LST rises across the entire LNC (Figure 1b), with the lake-wide averaged value increased to 10.85°C from 8.35°C during June–July. Moreover, LST increases from west to east, and the modeled circulation features eastward flow in the main basin and an anti-cyclonic gyre in the eastern basin. In October–November, the lake-wide averaged LST drops to 7.30°C, accompanied by a more pronounced eastward increasing LST and eastward surface flow (Figure 1c).

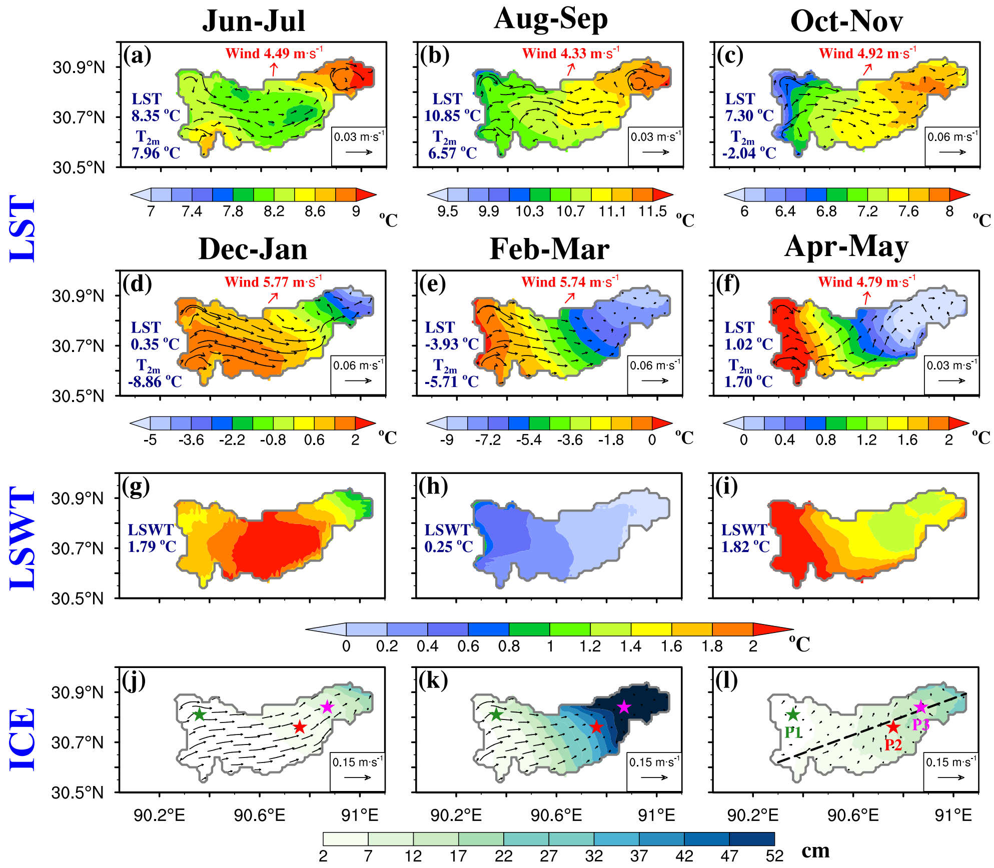

Figure 1. Top two rows: Bimonthly evolution of modeled lake surface temperature (LST, color shading) averaged over 2007–2017. Third row: Same as the second row, but for the lake water surface temperature (LSWT). Bottom row: same as the second row, but for the effective ice thickness (color shading) and drift (vectors). In the top three rows, vectors denote the water currents averaged over the surface layers (0–3 m), texts denote the lake-wide averaged LST, LSWT, 2-m air temperature (T_{2m}) and surface wind. In (l): Dashed line denotes the southwest-northeast transection used in Figure 5; Asterisks from west to east denote the selected sites P1 (30.81°N, 90.36°E), P2 (30.76°N, 90.76°E), and P3 (30.84°N, 90.87°E), with the respective water depth of 51, 92, and 51 m, for analysis shown in Table 1, and Figures 3, 6 and 10.

From December to May, LNC enters its ice-covered phase, with the LST being lower than LSWT (Figures 1d–1l). The prevailing southwesterly winds drive consistent eastward surface water movements and ice drift. In December–January, the lake-wide averaged LST (LSWT) drops to 0.35 (1.79) °C. The lake ice first forms in the eastern basin (Figure 1j), where the LST shows large negative values and increases westward (Figure 1d). The LSWT shows an offshore-nearshore gradient, as the greater thermal inertia of deeper waters resists and delays convective cooling (Figure 1g). The LSWT spatial pattern is reversed from the LST in October–November, when the warmer water accumulates in the eastern basin due to prevailing winds (Figure 1c). In February–March, the lake ice expands westward to nearly cover the entire LNC with the ice thickness decreasing westward (Figure 1k). The LST and LSWT also decrease westward (Figures 1e and 1h), and the lake-wide averaged LST (LSWT) decreases to −3.93 (0.25) °C. In April–May, lake ice decays from west to east, with the western LNC being ice-free first (Figure 1l). The lake-wide averaged LST (LSWT) rises to 1.02 (1.82) °C, and both LST and LSWT are higher in the western LNC (Figures 1f and 1i).

The seasonal LST/LSWT variations can be further related to the lake column heat balance in LNC, with the spatial maps of heat budget components shown in Figure 2 and at the central lake point P2 (30.76°N, 90.76°E) shown in Figure 3.

In June–July, the lake heat storage increases, corresponding to the positive $SNHF_{\downarrow}$ (Figures 2a and 2b). Due to the differential heating mechanism (Monismith et al., 1990), LST rises more rapidly over shallower areas than over deeper ones, leading to a cross-isobath LST gradient. This gradient facilitates temperature diffusion and

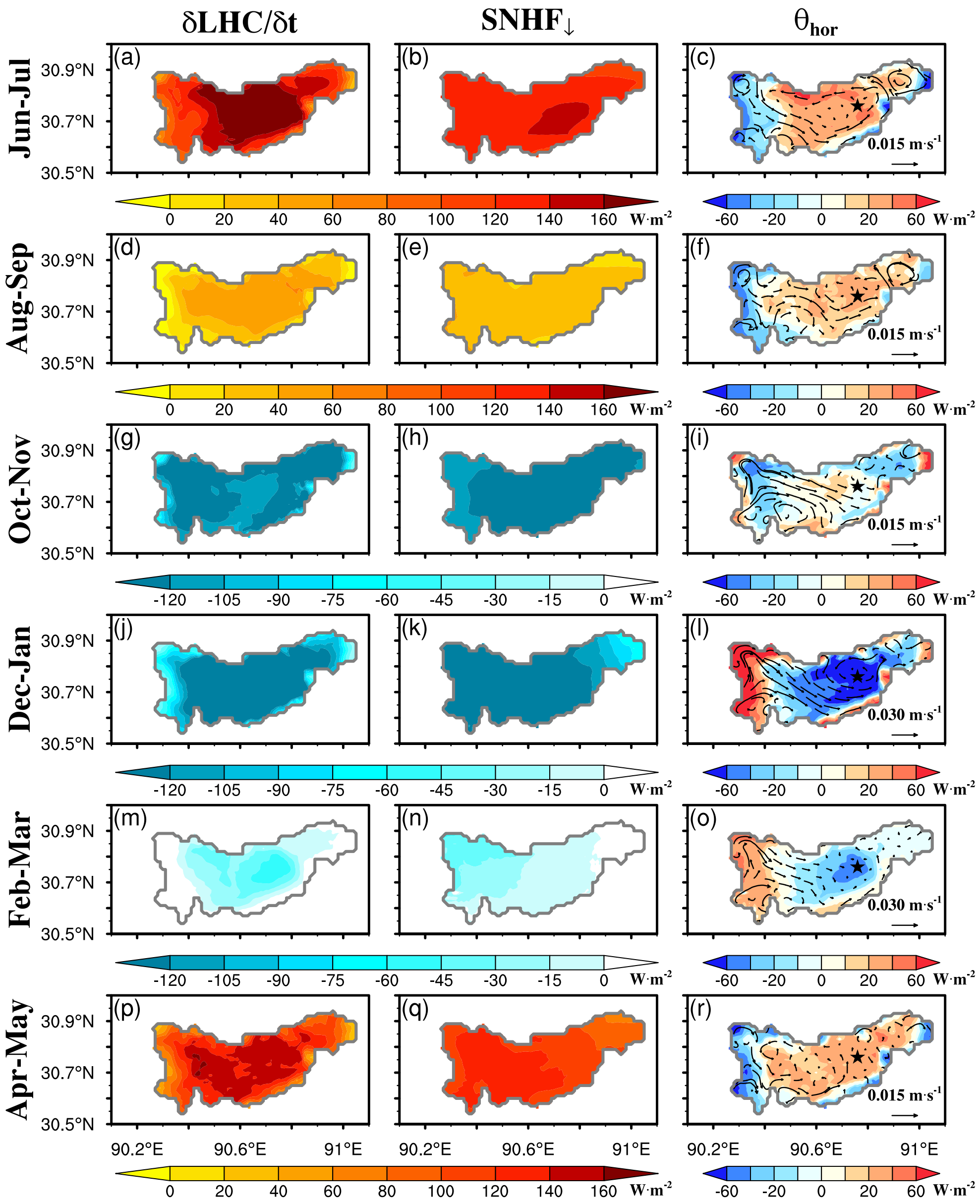

Figure 2. The bimonthly averaged heat budget components (unit: W·m^{-2}) based on ICEPOM simulations during 2007–2017: (left column) rate of change in lake heat content $\delta LHC/\delta t$, (middle column) surface net heat flux $SNHF_{\downarrow}$, and (right column) horizontal heat exchange θ_{hor}. In the right column, the vectors represent the depth-averaged currents, and the asterisk denotes the location of P2.

baroclinic circulation (a response to temperature-dependent density gradients) (Beletsky & Schwab, 2001; Boyce et al., 1989; Rao et al., 2004). In lakes such as LNC where the earth's rotation takes effect, the depth-averaged currents feature a cyclonic gyre in the main basin, while an anti-cyclonic gyre presents in the eastern basin. The convergence of depth-integrated horizontal heat flux θ_{hor} is positive within the mid-lake gyre and negative along the western and southeastern coasts (Figure 2c). This indicates that heat is laterally transported from the shallower coastal areas to the central lake regions, acting to weaken the nearshore-offshore thermal contrast. At P2, θ_{hor} accounts for ~23% of the bimonthly increase in lake column heat content (Figure 3). In August–September, the positive $SNHF_{\downarrow}$ decreases across the whole LNC (Figure 2e), corresponding to a smaller rate of heat storage increase (Figure 2d) compared to June–July. The depth-averaged currents feature eastward flow in the main basin and several small-scale gyres over shallower areas (Figure 2f). The lateral processes transport heat from the western coast eastward; and at P2, θ_{hor} contributes to ~43% of heat content increase (Figure 3). Given the

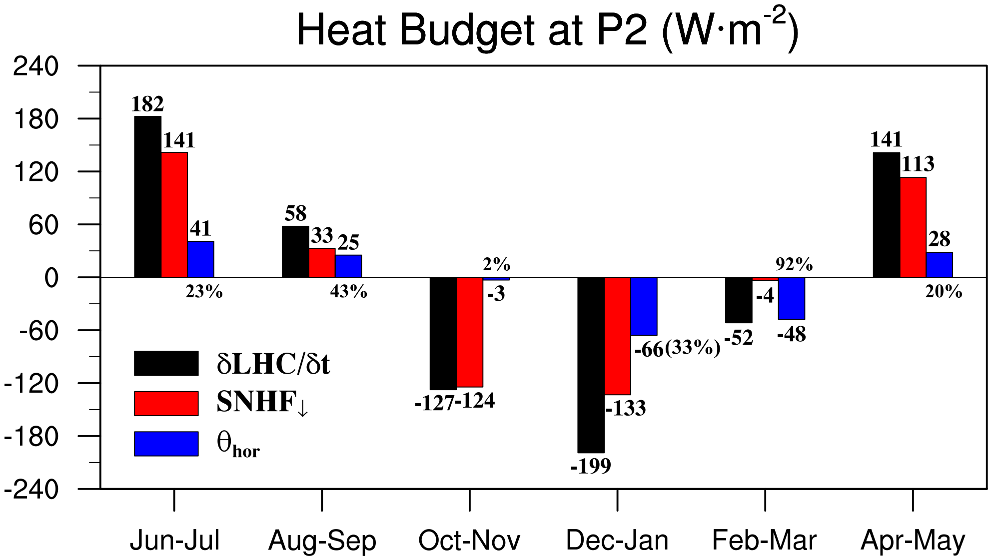

Figure 3. Same as Figure 2, but for the heat budget at the central lake point P2. The values of $\delta\text{LHC}/\delta t$, $\text{SNHF}_{\downarrow}$, θ_{hor} and the percentage of θ_{hor} over $\delta\text{LHC}/\delta t$ are given in texts.

nearly spatially uniform $\text{SNHF}_{\downarrow}$, the eastward heat transport must be the main driving factor for the eastward increasing LST pattern during this phase. In October–November, $\text{SNHF}_{\downarrow}$ over LNC becomes negative due to the reduced net radiation and increased latent and sensible heat loss associated with the strong positive lake-air temperature/humidity differences (Figure 2h). The modeled lake heat storage decreases (Figure 2g), marking the onset of autumnal cooling. The surface and depth-averaged currents have similar patterns, featured by strong flows turning off the western coast and then directing southeastward (Figures 1c and 2i). This corresponds to the negative (positive) θ_{hor} in the western (central) lake, which helps maintain the eastward increasing LST.

From the preceding December to May, lake ice has large influences on the lake-air heat/momentum fluxes and the spatial variability of LST/LSWT. That is, heavily ice-covered regions correspond to areas with lower LST/LSWT, smaller absolute value of $\text{SNHF}_{\downarrow}$, and weaker water flows (Figures 1d–1l and 2j–2r). In this phase, besides the ice cover, the lateral heat transport is another important determinant of LSWT spatial variability. In December–January, the persistent surface heat loss causes a further decline in lake heat storage and temperature (Figures 2j and 2k). However, in the deep central basin, the epilimnion cools more slowly due to the wind- and density-driven vertical convection, which mixes the cold epilimnion with the warmer hypolimnion, mitigating surface heat loss. This explains the nearshore-offshore LSWT gradient shown in Figure 1g. Surface and depth-averaged circulations (Figures 1d and 2l) resemble those in October–November, but become stronger with the intensified southwesterly wind (Figure 1d). θ_{hor} shows large positive values along the western coast and negative values in the central and eastern regions, due to coastal upwelling and the eastward aggregation of cold water. The lateral heat transport processes accelerate water cooling in the central and eastern LNC, favoring the formation of ice. At P2, θ_{hor} contributes ~33% of the bimonthly decrease in lake column heat content (Figure 3). In February–March, the spatial patterns of circulation and θ_{hor} remain similar to those in December–January, but with reduced magnitude (Figure 2o), especially over the central and eastern regions covered by packed ice. Because the ice presence substantially inhibits $\text{SNHF}_{\downarrow}$, the lateral heat transport makes dominant contributions to the changes in lake column heat content (Figures 2n and 2o), accounting for ~92% of the bimonthly heat loss at P2 (Figure 3), and eventually leads to the westward increase of LSWT (Figure 1h). By April–May, $\text{SNHF}_{\downarrow}$ has larger positive values and LST/LSWT increase in the less ice-covered western LNC (Figures 1f, 1i, and 2q), where the surface lake circulation becomes stronger (Figure 1f) while the depth-averaged flow is still weak (Figure 2r). The related lateral heat transport from the coastal regions contributes to lake warming and ice ablation in the central and eastern lake basins (Figure 2r), and θ_{hor} contributes to ~20% of the bimonthly increase in lake column heat content at P2 (Figure 3).

The above analyses reveal that the lateral heat transport and freeze-thaw processes are crucial for determining the pronounced horizontal variability of LST/LSWT in LNC. Here, we examine the temporal variations of lake-wide

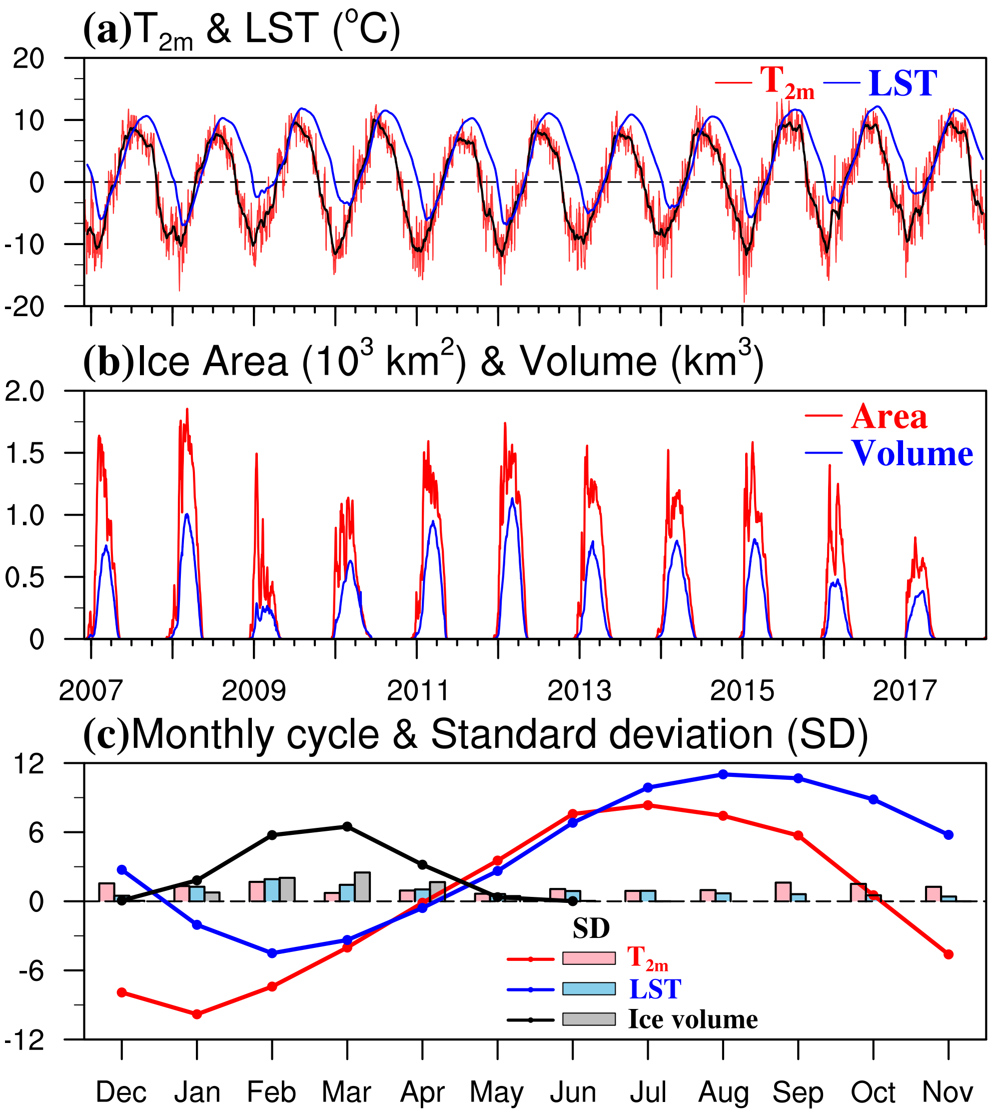

Figure 4. Time series (a) of 30-day running means of lake-wide averaged T_{2m} (black curve) and modeled LST (blue curve), overlaid with daily over-lake T_{2m} (red curve), and (b) Modeled daily lake-wide averaged ice area (red curve) and volume (blue curve) during 2007–2017. (c) The monthly over-lake T_{2m} (°C, red curve) and modeled LST (°C, blue curve) and ice volume (10^{-1} km^3, black curve) averaged during 2007–2017, with the bars denoting the standard deviation (SD) of monthly means across the 11 years.

averaged LST. Based on time series of lake-wide averaged 2-m air temperature (T_{2m}), LST, ice area and volume during 2007–2017 (Figures 4a and 4b), the monthly climatology of these parameters as well as the standard deviations of the monthly means across the 11 years are obtained (Figure 4c). During March–June when lake ice is melting, LST continually rises and remains closely aligned with the over-lake T_{2m}. During the rest months, LST consistently exceeds T_{2m}. This notable positive lake-air temperature difference during August–January favors an unstable atmospheric boundary layer. The evident seasonal cycle of LST (maximum 11.02°C in August and minimum −4.51°C in February) lags that of T_{2m} by about 1 month. The temporal correlation (TC) between daily LST and T_{2m} reaches a maximum of 0.98 when LST lags T_{2m} by 39 days. The hysteresis response of LST to T_{2m} is consistent with the findings from 2-year in situ observations in LNC reported by Wang et al. (2019). Similar hysteresis relationship between LST and T_{2m} has also been reported for other large lakes, for example, Lake Superior and Lake Baikal (Bai et al., 2013; Toffolon et al., 2014), which was ascribed to large lake thermal inertia, delaying both the warming and cooling processes. Additionally, due to the "cumulative effects" of T_{2m} in different preceding months, the seasonal variation of ice also shows a phase lag with T_{2m}. The ice-on date, maximal ice volume and ice-off date occur significantly later relative to when T_{2m} drops below 0°C, reaches the minimum, and rises to above 0°C, respectively (Figure 4c). Moreover, in terms of the interannual standard deviations during the ice formation phase (December–March), the occurrence of larger values for LST and ice volume (January–March) also lags that for T_{2m} (December–February). This further confirms the strong coupling between LST and ice variations, and their seasonal hysteresis response to T_{2m}.

4.2. Lake Thermal Structure

This section examines the seasonal progression of vertical-horizontal structure of lake water temperature based on simulations averaged over 2007–2017. Figure 5 shows the monthly water temperature along a southwest-northeast transection (depicted in Figure 1l), as well as the horizontal currents normal to the transection. Figure 6 shows the daily time series of the effective ice thickness and water temperature profiles at the western (P1), central (P2) and eastern (P3) locations (positions depicted in Figure 1l). The phenological characteristics of warm thermal stratification and autumnal overturning at these locations are summarized in Table 1.

During June–November, LNC is ice-free and stably stratified with warmer water lying above the colder water at temperatures exceeding T_{dmax} (Figures 5a–5f). A basin-wide warm thermal stratification develops across the entire LNC in June (Figure 5a), with onset dates at P1, P2 and P3 on 28th May, 8th June, and 2nd June, respectively (Figure 6 and Table 1). Compared to the deeper central lake, shallower regions stratify earlier and feature a warmer and deeper mixed layer. The thermocline is dome-shaped, and there exists a pronounced nearshore-offshore temperature gradient in the upper 20-m layer (Figure 5a). In July and August, the epilimnion further warms and deepens, leading to a relatively flat thermocline (Figures 5b and 5c). In September, as the lake-air temperature difference increases (Figure 4c) and wind strengthens (to be discussed around Figure 8c), turbulent mixing and surface heat loss intensify. These factors, together with the weakening solar radiation, contribute to the onset of lake destratification. By October, the epilimnion temperature decreases significantly, and the mixed layer deepens (Figure 5e). At this stage, the thermocline tilts upward toward the western coast, and a west-east temperature gradient persists within the mixed layer (Figure 5e), indicating coastal upwelling and eastward warm water transport driven by the prevailing southwesterly wind. In November, the western LNC first becomes fully mixed, while the central-east lake remains weakly stratified, and the thermocline deepens to ∼50 m (Figure 5f). The end dates of warm thermal stratification at P1, P2 and P3 are 26th October, 20th November and 5th November, respectively (Figure 6 and Table 1). Lake destratification shows evident intra-lake heterogeneity due to the combined effects of depth-dependent thermal inertia and horizontal heat redistribution via lateral processes.

Further surface cooling leads to the lake overturning and successive formation of inverse thermal stratification and ice. The autumnal overturning lasts about 1 month, during which a thermal bar initially forms in coastal regions and then propagates toward the central lake (Figure 5g). The thermal bar is a narrow water zone with a temperature of T_{dmax}, which features convergent downward motions, and acts as a barrier separating the stratified nearshore from well-mixed offshore waters. It forms in response to density-driven convection induced by surface cooling during autumn or radiative heating during spring (Boyce et al., 1989; Rao et al., 2004; Tikhomirov, 1963) and is commonly observed in many large temperate lakes worldwide (Blokhina & Selin, 2019; Tsydenov, 2019). In December, LNC transitions into an inversely stratified state, with colder water at temperatures below T_{dmax} overlying warmer water (Figure 5g). The onset dates of inverse thermal stratification at P1, P2 and P3 are 3rd December, 19th December, and 11th December, respectively (Figure 6 and Table 1). Shallower coastal regions stratify earlier, and the thermocline has a pronounced dome shape. From January to March, the upper layer progressively cools and deepens, accompanied by increasing ice thickness (Figures 5h–5j and 6). The isotherms tilt upward in western LNC but downward in the heavily ice-covered eastern LNC, with the cold epilimnion gradually thickening until it nearly covers the entire lake column by March. This can be primarily attributed to coastal upwelling and eastward transport of surface cold water, driven by the prevailing southwesterly wind. Note that even in March with maximal ice coverage, the deeper layer in the central basin remains above 1°C. During April–May, the resumed radiation and T_{2m} cause ice ablation. The related decrease in surface albedo and weakened ice insulation effect favor the penetrating of radiative heating and wind mixing into the water column. By the end of ice-covered phase, the lake is again mixed from top to bottom (Figure 6). The ice-off dates at P1, P2 and P3 are 28th April, 12th May, and 20th May, respectively (Table 1). Because the western shallower regions enter the open-water phase first, the water column there warms at a faster rate and stratifies earlier compared to the central and eastern LNC, which still feature a well-mixed cold pool with temperatures below T_{dmax} in May

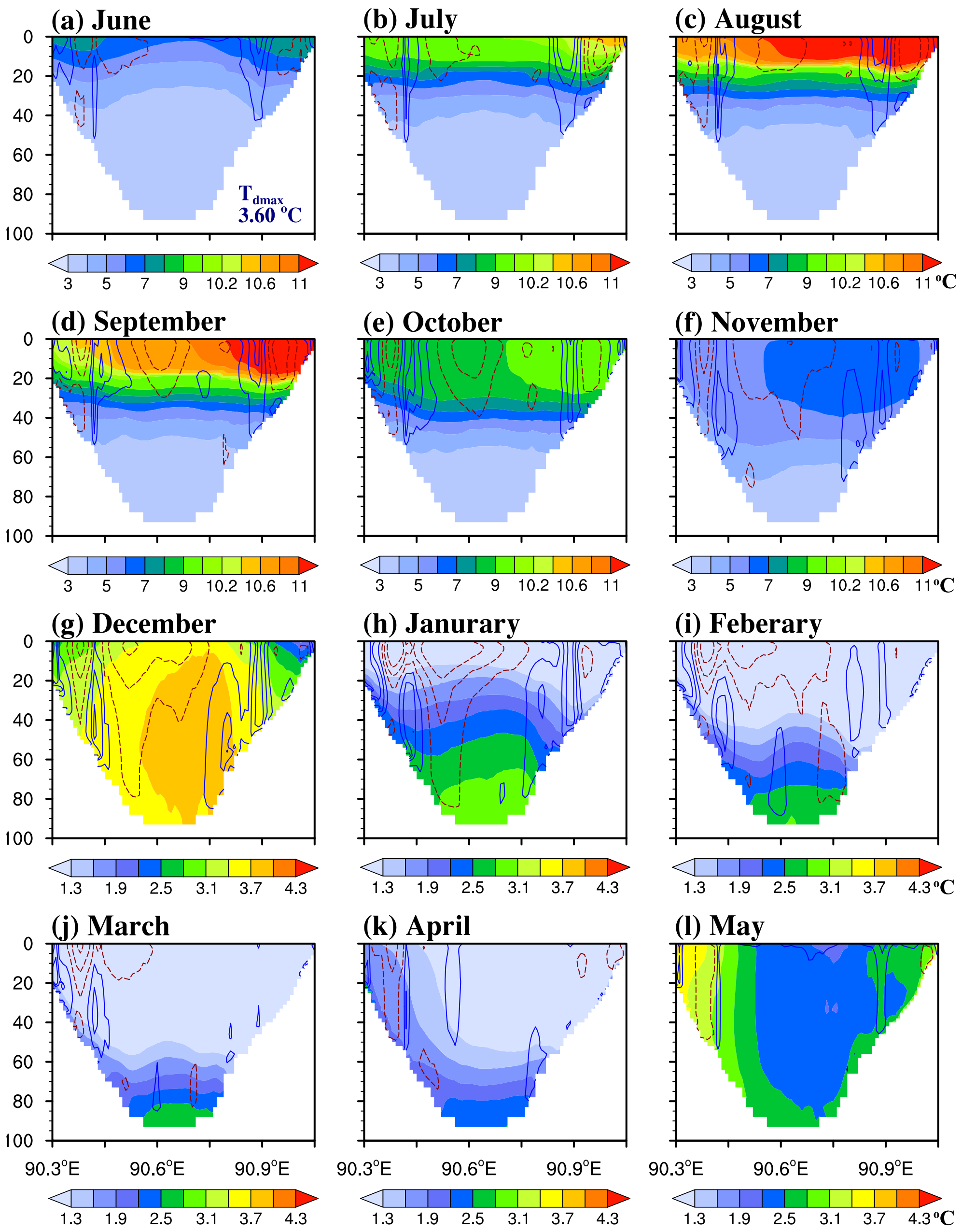

Figure 5. Monthly evolution of modeled lake temperature (shaded) along the southwest-northeast transection (depicted in Figure 11), overlaid with the horizontal currents (contours) normal to the transection. The contours have an interval of 0.01 m s^{-1}, with solid (dashed) contours denoting currents in northwestward (southeastward) direction. T_{dmax} denotes the "temperature of maximum water density" and is estimated to be 3.60°C with a surface pressure of 0.57 bar and a salinity of 1.7 g L^{-1} for Lake Nam Co.

(Figure 5l). The spring thermal bar occurs between the stratified and thermally homogeneous areas, and will propagate across the lake until the establishment of summer thermal stratification.

4.3. Lake Circulation

In our previous study, POM was used to simulate lake thermo-hydrodynamics during May–December 2013 (Wu et al., 2021). Without including an ice component, the model simulations revealed a predominant mid-lake cyclonic gyre throughout this ice-free phase, along with pronounced offshore currents and upwelling along the western coast during September–December. A series of sensitivity experiments were conducted to understand the

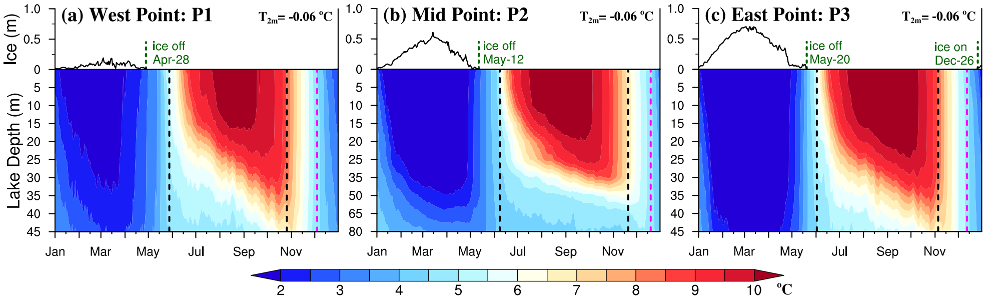

Figure 6. Seasonal evolution of vertical profiles of the daily lake water temperature (color shading) and the effective ice thickness (curves) averaged during 2007–2017at P1, P2 and P3 (locations denoted in Figures 1j–1l). The black text denotes the annual mean of lake-wide averaged T_{2m}; texts and dashed lines in green denote the ice-on and ice-off dates; dashed black lines denote the onset and end dates of warm thermal stratification; and dashed magenta lines denote the end of autumnal overturning.

forcing mechanisms of the circulation. The results indicated that the prevailing southwesterly winds are the primary driving factor for lake circulation, and the positive wind stress curl, surface heat flux and thermal stratification make a secondary contribution to enhance the cyclonic flow in the main basin.

In this study, the implementation of ICEPOM enables the simulation of ice-covered season and hence facilitates multi-year simulations. Figure 7 shows the monthly depth-averaged water currents and water level from ICEPOM simulations averaged during 2007–2017. During the ice-free phase, the circulation pattern is consistent with that simulated by Wu et al. (2021), featuring a mid-lake cyclonic gyre from June to August (Figures 7a–7c), and strong jets and upwelling along the western coast from September to November (Figures 7d–7f). This can be explained by the mechanisms discussed by Wu et al. (2021). However, several notable differences emerge between the present and previous simulations. First, in May, the well-developed nearshore-offshore thermal gradient and mid-lake cyclonic gyre produced by POM are weaker and primarily confined to the western ice-free region in the ICEPOM simulation (Figures 5l and 7l). This discrepancy arises because, unlike the ice-uncoupled POM, ICEPOM realistically reproduces the observed eastward progression of lake ice melt, with the eastern basin remaining ice-covered in early May (Gou et al., 2017; Qu et al., 2012). The presence of lake ice insulates the water surface from receiving wind stress and solar radiation, leading to the formation of cold pool and weakened circulation in the eastern basin. In Wu et al. (2023), a pair of sensitivity experiments conducted using ICEPOM, with and without the inclusion of the ice component, further confirmed the critical role of lake ice in modulating the spring radiative heating and water movements, and underscored the added value of ice coupling for realistically simulating the lake thermal-hydrodynamic processes. Second, in contrast to the mid-lake cyclonic circulation pattern from both POM and ICEPOM solutions for September–October 2013, the long-term mean circulation in the main basin shows two weak counterrotating cells in September and a single pronounced anti-cyclonic gyre in the western LNC during October (Figures 7d and 7e). This suggests the presence of year-to-year changes in the autumn lake circulation, which can be ascribed to wind variations (to be discussed in Section 5.3).

Table 1

Statistics of the Warm Thermal Stratification and Autumnal Overturning Diagnosed From ICEPOM Simulations at Three Selected Points Shown in Figure 1

	Warm thermal stratification		
Points	Onset	End	Duration (Days)
P1	28th May	26th October	152
P2	8th June	20th November	166
P3	2nd June	5th November	157
	Autumnal overturning		
Points	Onset	End	Duration (Days)
P1	26th October	3rd December	39
P2	20th November	19th December	30
P3	5th November	11th December	37

At the early stage of ice formation (December–January), spatial distributions of water level and currents remain largely consistent with those in November, except for stronger mid-lake cyclonic motion and alongshore jets (Figures 7g and 7h). This change is related to the further strengthening of the southwesterly wind and an increased water level gradient between the central and eastern regions. Unlike the surface-confined circulation during the warm stratified season, horizontal currents extend throughout the water column during this phase (Figure 5). During February–March, both the water level gradient and circulation in the central-east LNC significantly weaken (Figures 7i and 7j), corresponding to the decreased thermal gradient, and also the thickened ice cover that dampens the wind stress input. Along the western coast, the northward offshore flow and depressed water level persist but get

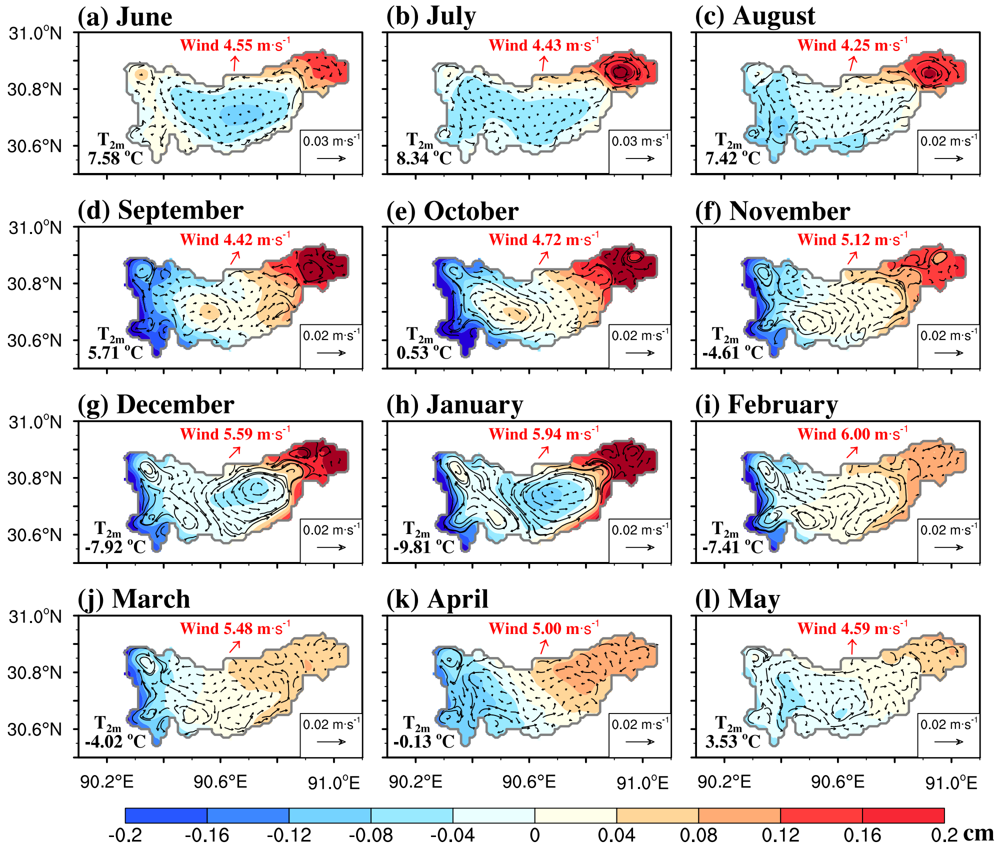

Figure 7. Monthly evolution of modeled lake water level (color shading) and depth-averaged currents (vectors) during 2007–2017. The formats of texts and arrows are the same as Figure 1.

evidently weaker by March than in previous months. In April, the depth-averaged circulation features a weak cyclonic flow in the western LNC, coinciding with the eastward increasing water level (Figure 7k).

Variations of the lake-wide averaged 10-m wind, ice drift and current speed during 2007–2017 are presented as 10-day running mean time series (Figure 8a), as well as the monthly seasonal cycle and standard deviations of the months means of wind speed and current speed over the 11 years (Figure 8b). Figure 9 presents the spatial distribution of monthly effective ice thickness, and the wind-water and ice-water stresses from the preceding December to May averaged over 2007–2017. The wind, ice drift and current speeds all show strong variability at synoptic and seasonal time scales (Figure 8a). During the ice-free season, the current speed is low during June–August and gradually increases during September–November, consistent with the seasonal changes of wind speed (Figures 8a and 8b). During the ice-covered phase, the changes of water flow are influenced by both wind and ice conditions. From December to January, lake-wide averaged current and ice drift speed increase with the wind speed, and the current speed reaches the annual maximum of 3.22 cm·s^{-1} (Figure 8b). Since the wind drag over the ice surface is considerably greater than over the water surface, the eastward drift of thin ice is more energetic, with its speed well above both the surface and depth-averaged current speeds (Figures 1d, 1j, and 8a). In January, the ice-water stress is predominantly northeastward across LNC, aligning with the northeastward wind-water stress to sustain the eastward surface water movement (Figures 1d, 9b, 9g, and 9h). Note that wind-water stress dominates the water movements, as it is approximately an order of magnitude larger than the ice-water stress. During February–March, the increased ice coverage significantly reduces the wind stress transmitted to the water surface, and also dampens the eastward ice drift and ice-water stress (Figures 9c–9d and 9g–9h). This effect is especially pronounced in the central-eastern LNC that is covered by the packed ice. The combined effects cause a sharp decline in lake-wide averaged current speed (Figure 8). In April the ice ablation begins, and the ice drift speed recovers (Figure 8a). Wind stress is again efficiently transferred to the water surface to drive the water

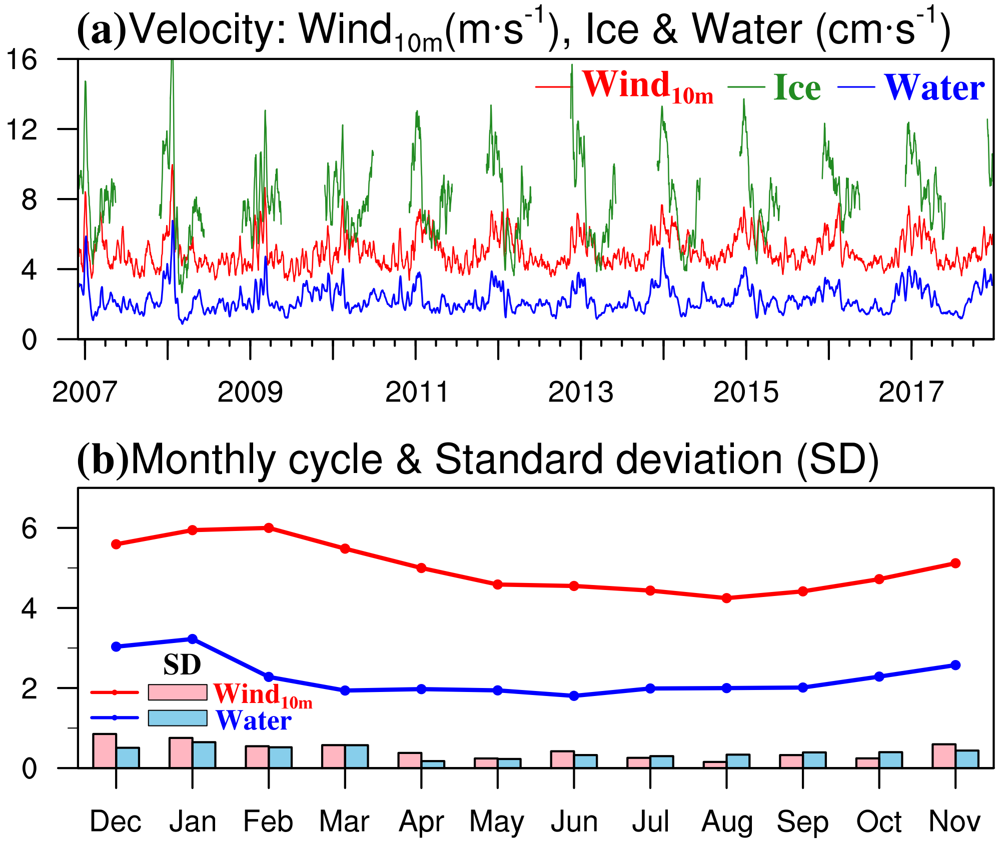

Figure 8. (a) 10-day running mean time series of the lake-wide averaged 10-m wind (red curve), ice drift (green curve), and depth-averaged currents (blue curve) speed during 2007–2017. (b) Monthly 10-m wind (red curve) and depth-averaged currents (blue curve) speed averaged during 2007–2017, with the bars denoting the standard deviations of monthly means across the 11 years.

movements (Figure 9e). However, due to the decrease of wind speed, the lake-wide averaged current speeds in April and May remain low (~0.19 cm·s^{-1}), comparable with the values in heavily ice-covered March.

5. Interannual Variations

5.1. Lake Thermodynamics

Besides the distinct seasonal cycle, the lake thermodynamics of LCN also exhibits significant interannual variations. Figure 10 shows the daily time series of the effective ice thickness and water temperature profiles at the central lake point (P2) during 2011 and 2017. For the annual mean of lake-wide averaged T_{2m}, the year of 2011 has a value of 1.23°C lower, whereas the year of 2017 has a value of 1.25°C higher, than the 2007–2017 average. Consequently, the ice condition at P2 is much lighter in 2017 than in 2011. Relative to 2011, in 2017 the mean effective ice thickness decreases from 0.30 to 0.16 m, the under-ice water temperature averaged over February–April increases from 0.43 to 1.03°C, and the ice-off date is advanced by 25 days from 22th May to 28th April (Figure 10). Additionally, compared to 2011, the onset of warm thermal stratification in 2017 occurs 13 days earlier from 16th June to 3rd June, and the thermal stratification is more stable with a warmer and deeper mixed layer.

Averaged over the entire LNC, Figure 11 shows the annual time series of LST, T_{2m} and ice volume, and Figure 12 shows the annual time series of the warm thermal stratification phenology, T_{2m} and ice-off date. During 2007–2017, the mean LST for the entire year (January–December), ice-covered phase (preceding December to following April), and ice-free phase (June–November) are 3.99°C, −1.55°C, and 8.83°C, respectively. The mean duration, onset and end of warm thermal stratification are 155 days, 4th June and 6th November, respectively. The annual LST during different phases shows significant interannual variations and high temporal correlations (TCs)

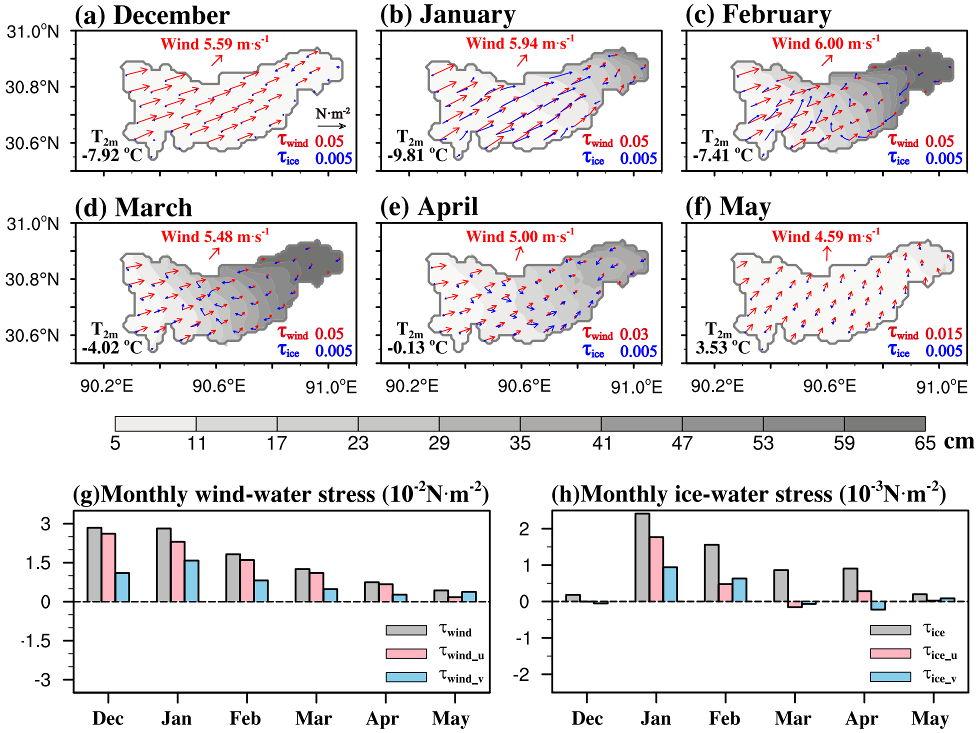

Figure 9. Top two rows: Monthly effective ice thickness (gray shading), wind-water stress (τ_{wind}, red vectors), and ice-water stress (τ_{ice}, blue vectors) from the preceding December to May, averaged over 2007–2017. The formats of texts and arrows are the same as Figure 1. Bottom row: Monthly lake-wide averaged (g) wind-water stress and (h) ice-water stress, with the light pink (blue) bars denoting the eastward (northward) component.

with the over-lake T_{2m} (Figures 11a–11c). The duration of warm thermal stratification, which is primarily governed by the vertical water density gradient linked to surface water temperatures, has a high TC value of 0.89 with T_{2m} (and 0.94 with LST) averaged over the ice-free months (June–November) (Figure 12a). In other words, higher T_{2m} values typically correspond to higher LST and longer warm stratified season.

From Figures 12b and 12c, warm thermal stratification onset (break-up) date has a correlation coefficient of −0.74 (0.73) with T_{2m} averaged over the previous ice-covered (ice-free) season. Higher T_{2m} in different preceding months corresponds to earlier onset and later break-up dates of the summer thermal stratification. Note that

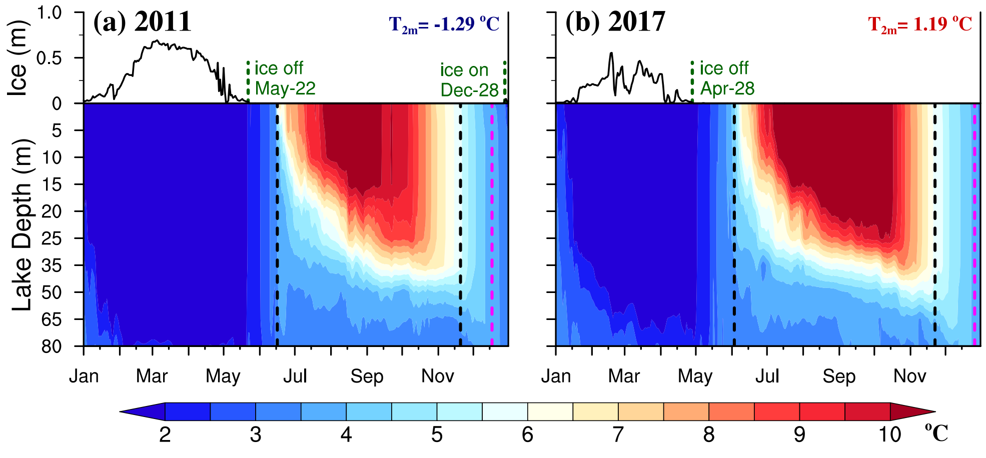

Figure 10. Same as Figure 6, but for the vertical lake thermodynamics at P2 during (a) 2011 and (b) 2017. Texts denote the annual mean of lake-wide averaged T_{2m}.

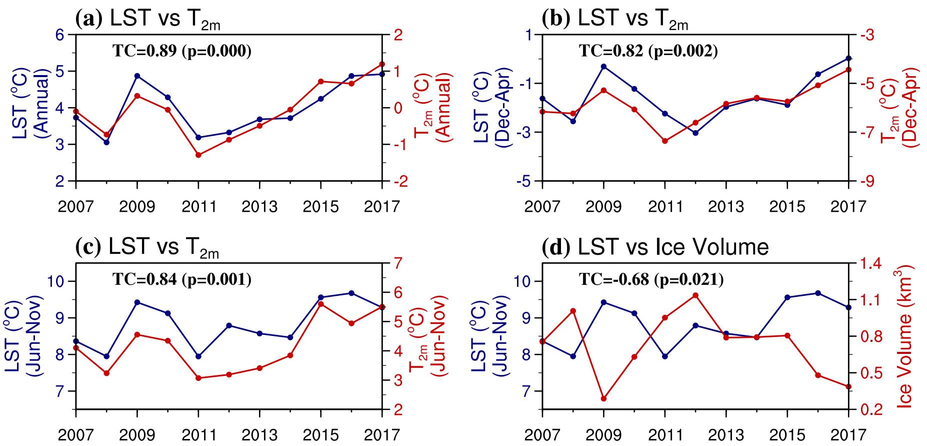

Figure 11. The annual time series of lake-wide averaged LST (blue curves) and over-lake T_{2m} (red curves) averaged during (a) January–December, (b) preceding December to following April, and (c) June–November. (d) Annual time series of lake-wide averaged LST (blue curve) averaged during June–November and ice volume (red curve).

the interannual variation of stratification onset is larger than that of stratification break-up. This can be attributed to the strong correspondence between ice-off and stratification onset dates (Figure 12d). For years with mild winters with reduced ice coverage, the stratification onset is considerably advanced due to the combined effects of the higher end-of-winter heat retention and earlier spring radiative heating. Consequently, as the stratification suppresses vertical mixing and causes a stronger LST response to T_{2m} variations, higher LST and longer stratified phase are expected in the following ice-free season. Thus, high TC values are found between the annual ice volume (mainly from January to May) and LST averaged over June–November (Figure 11d), and between ice-off dates and stratification onset dates (Figure 12d). Such relationships between lake ice variations and thermal response have been well-documented for seasonally ice-covered lakes worldwide, that is, Laurentian Great Lakes and Lake Vättern (Austin & Colman, 2007; Weyhenmeyer et al., 2007; Zhong et al., 2016). Furthermore, this process may exacerbate the impact of climate warming on lake water temperature, thermal stratification, and mixing regimes via positive ice-albedo feedback (Huang et al., 2022; Li et al., 2022; Pilla & Williamson, 2021; Wu et al., 2024).

5.2. Lake Circulation During the Ice-Covered Phase

In Section 4.3, wind and ice conditions are identified as the main drivers of the seasonal variation of lake circulations during the ice-covered phase. This conclusion also holds for the interannual variation of lake circulation. Figure 13 shows the horizontal distributions of water level, depth-averaged currents, and ice conditions during the

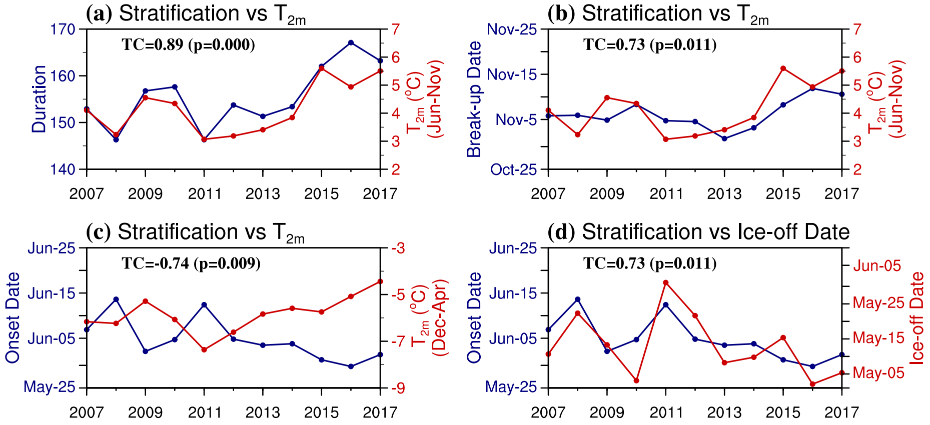

Figure 12. Blue curves: annual time series of the lake-wide averaged warm thermal stratification (a) duration, (b) break-up date, and (c)–(d) onset date during 2007–2017. Red curves: annual time series of the over-lake T_{2m} during (a)–(b) June–November and (c) preceding December to following April, and (d) ice-off date.

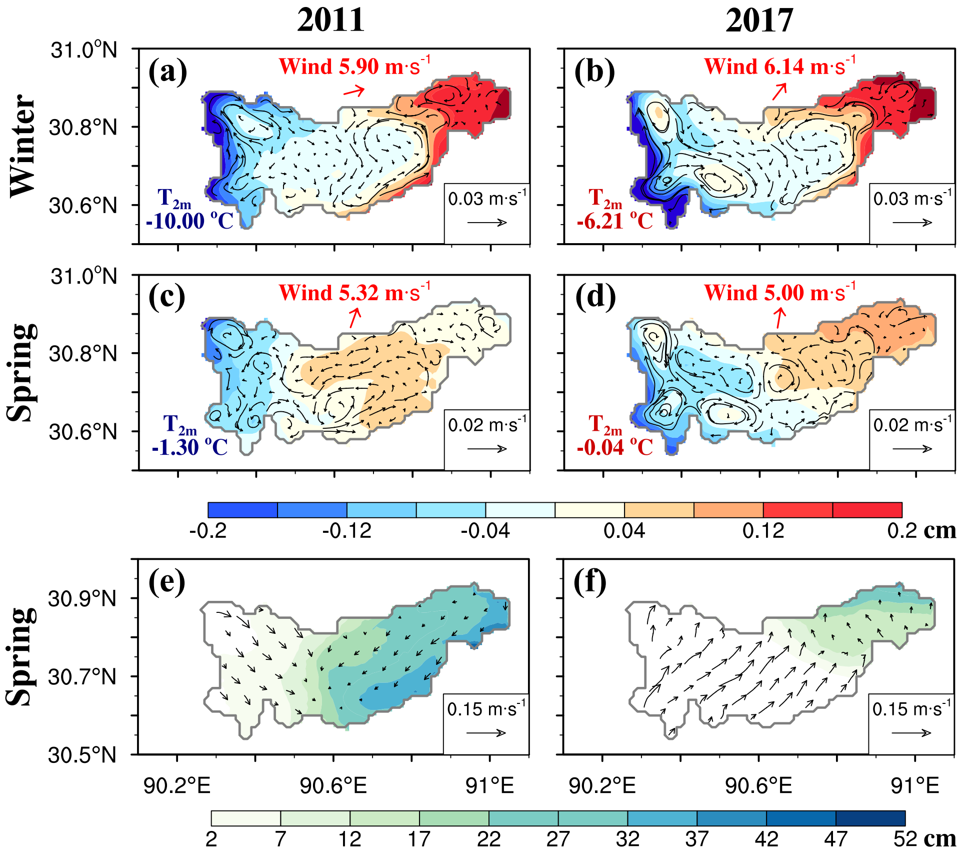

Figure 13. Top two rows: Spatial distributions of modeled lake water level (color shading) and depth-averaged currents (vectors) during the winter and spring of 2011 and 2017. Third row: Same as the second row, but for the effective ice thickness (color shading) and ice drift (vectors). In panels (a)–(d), the formats of texts and arrows are the same as Figure 1.

winter and spring of 2011 and 2017. Figure 14 shows the statistics of the daily surface wind direction and speed during the winter and spring of 2011–2017, and the interannual variations of the depth-averaged current speed, wind speed, and effective ice thickness. In winter the over-lake winds are prevailingly southwesterly (Figure 14a), the lake circulation patterns show minimal year-to-year variations (Figures 13a and 13b). However, interannual variations of lake-wide averaged current speed and wind speed are significantly correlated (TC = 0.72) (Figure 14c). For example, compared to 2011, the winter of 2017 experiences stronger alongshore jets, coastal Ekman upwelling (indicated by the depressed water level along the western shore), and mid-lake gyre, associated with the larger lake-wide averaged wind speed (Figures 13a and 13b). During the winter months of December and January, the lake ice is relatively thin and primarily confined in the eastern basin (Figure 1j), hence the impact of ice on winter lake circulation is minimal. The annual time series of the lake-wide averaged current speed and effective ice thickness have a very low TC value (0.07), confirming that wind forcing dominates lake circulation in winter.

In spring, the decreased southwesterly wind and increased ice coverage lead to the weakened lake circulation compared to the previous winter (Figure 13). The annual time series of the lake-wide averaged current speed has a lower TC value (0.39) with the surface wind speed, but a higher TC value (−0.67) with the effective ice thickness (Figure 14d). This suggests that the interannual variability of ice condition has a strong impact on that of the spring circulation intensity. For example, in spring of 2017, while the wind speed is lower than 2011, the lake circulation is more energetic due to the lower ice coverage (Figures 13c–13f). Moreover, in the less ice-covered western basin, the circulation patterns in spring of both years are similar with that in the corresponding previous winter. This further underscores the impact of ice extent on spring circulation dynamics.

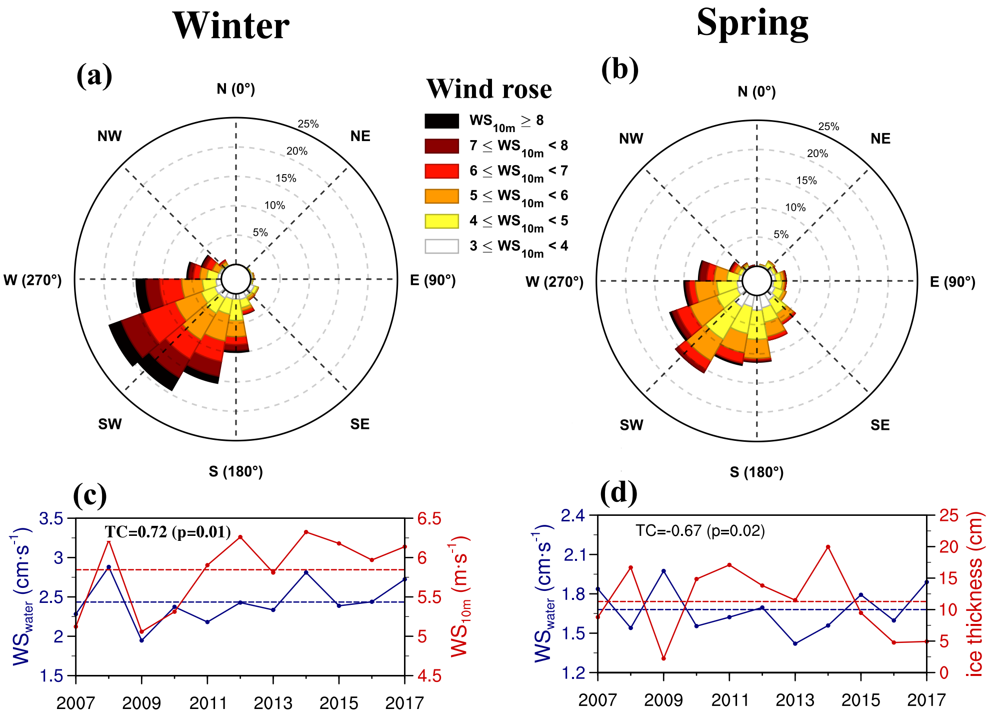

Figure 14. Wind roses for the daily lake-wide averaged surface wind during the (a) winter and (b) spring of 2007–2017. (c) The annual time series of the lake-wide averaged depth-mean current speed (WS_{water}, blue curve) and surface wind speed (WS_{10m}, red curve) during the winter of 2007–2017, overlaid with their 11-year means (dashed lines). (d) Is the same as (c), but for the WS_{water} and effective ice thickness during the spring of 2007–2017. In the top row, bar direction, length, and color denote the wind direction, occurrence frequency of the wind within a certain direction, and wind speed, respectively.

5.3. Lake Circulation During the Ice-Free Phase

Figure 15 shows the wind roses of the daily lake-wide averaged surface wind, and the interannual variations of the wind stress curl and current vorticity averaged over the central lake (30.62–30.82°N, 90.40–90.80°E) during the summer and autumn of 2007–2017. In autumn the over-lake winds are strong and prevailingly southwesterly with the dominant negative wind stress curl. In summer the over-lake winds are considerably weaker and exhibit greater variability in direction, with the wind stress curl fluctuating between positive and negative values. The interannual variation of the mid-lake current vorticity well follows that of the wind stress curl (Figures 15c and 15d), indicating that the wind stress curl serves as an effective source of current vorticity and impacts the lake thermodynamics through the Ekman pumping mechanism (Gill, 1982). Specifically, anticyclonic wind stress (negative curl) tends to induce near-surface convergence, downward Ekman transport, thermocline depression, and anticyclonic circulation. This effect is anticipated to be more pronounced during autumn when a large negative wind stress curl is present and results in stronger interannual variations of circulation.

Figure 16 shows the horizontal distributions of the water level and depth-averaged currents during the summer and autumn of 2010, 2014, 2009, and 2017. During the summers of 2010 and 2014, the wind stress curl over the central lake is positive (Figure 15a). This promotes Ekman pumping and near-surface divergence, working in concert with the prevailing southwesterly and thermal gradients to induce the pronounced basin-scale cyclonic circulation (Figures 16a and 16c). The cyclonic gyre persists into autumn but weakens due to the decreased thermal gradients (Figures 16b and 16d). Similar patterns of the wind stress and lake circulation also present in the summers and autumns of 2008, 2011 and 2013 (figures not shown). In the summers of 2007, 2009, 2015, 2016, and 2017, the prevailing southwesterly wind is interrupted, and the mid-lake wind stress curl approaches or falls below zero (Figure 15a). This disruption counteracts the effect of thermal gradients to weaken or completely modify the cyclonic circulation. Notably, in the summer of 2009, the mid-lake circulation is primarily anticyclonic, corresponding to the strong negative wind stress curl (Figures 15c and 16e). By autumn, as the effect of thermal gradients weakens and the negative wind stress curl intensifies, the central-west lake presents the

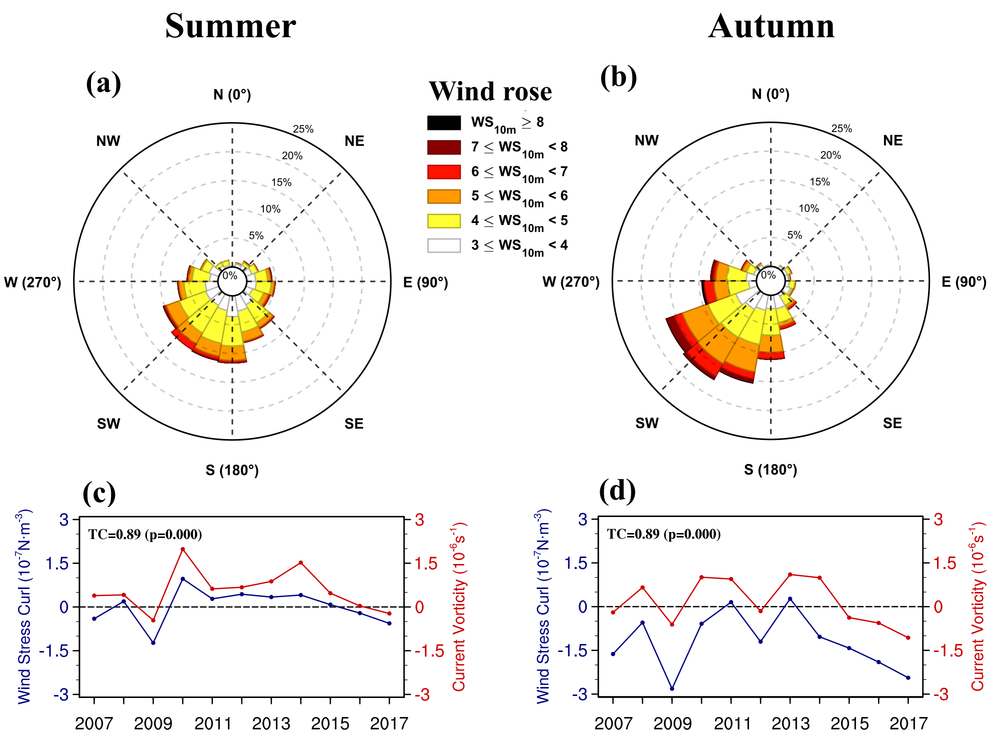

Figure 15. Wind roses for the daily lake-wide averaged surface wind during the (a) summer and (b) autumn of 2007–2017. The annual time series of wind stress curl (blue curves) and the vorticity of depth-averaged currents (red curves) in the central lake (30.62–30.82°N, 90.40–90.80°E) during the (c) summer and (d) autumn of 2007–2017.

pronounced wind-driven near-surface convergence, water level elevation, and the anti-cyclonic gyre (Figure 16f). The similar situation presents in the summer and autumn of 2017 (Figures 16g and 16h).

6. Summary and Discussion

In this study, a 3-D ice-hydrodynamic model is applied to investigate the thermo-hydrodynamics in LNC during 2007–2017, with a focus on its seasonal and interannual variations and the underlying mechanisms. Seasonally, LNC starts being thermally stratified since summer, presents destratification and turn-overs in late autumn, is frozen up and inversely stratified in winter, and turns over again in late spring of the following year. The lake thermodynamics features pronounced horizontal variability, primarily driven by the lateral heat transport and ice freeze-thaw processes, as revealed by a heat budget analysis. Interannually, LST and phenology of the warm thermal stratification (duration, onset and end date) show significant variability and correspondence with T_{2m} and ice conditions. The ice conditions in previous winter-spring influence the warm thermal stratification and LST during the following ice-free season (June–November). This process includes a positive ice-albedo feedback, that is, the declined ice cover lowers the surface albedo and weakens the insulation effect, leading to the increased solar radiation absorption, earlier stratification onset, enhanced lake warming, and a prolonged and more stable stratified phase than that due to the increased T_{2m} alone. This feedback mechanism leads to stronger seasonal and interannual variability of the thermodynamics of TP lakes compared to temperate lakes. This also leads to faster changes of TP lakes responding to the rapid surface air warming over TP (Cai et al., 2019; Yao et al., 2019).

The lake circulation presents a predominant mid-lake cyclonic gyre, upwelling along the western coast, and strong coastal currents during December–January. These circulation patterns are weakened considerably during February–April, due to the inhibition effect of the increased ice coverage on wind stress input. During winter-spring, the circulation pattern is consistent throughout 2007–2017 due to the prevailing southwesterly wind. However, the current speed shows evident year-to-year changes and significant correlations with the wind speed and ice conditions. That is, higher wind speed and less ice cover correspond to more energetic lake circulation during winter-spring.

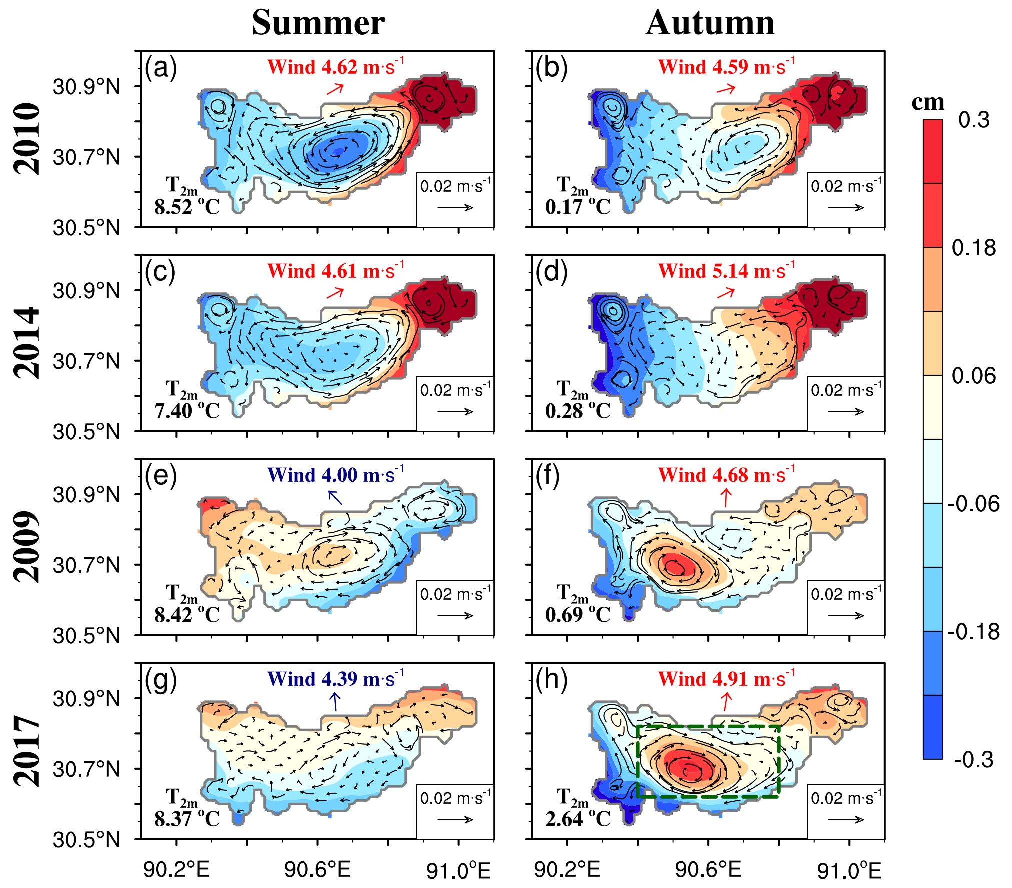

Figure 16. Spatial distributions of the modeled lake water level (color shading) and depth-averaged currents (vectors) during the summer and autumn of 2010, 2014, 2009 and 2017. The formats of texts and arrows are the same as Figure 1. In (h), the green rectangle box outlines the central lake region (30.62–30.82°N, 90.40–90.80°E) used for the analysis shown in Figures 15c and 15d.

Compared to winter-spring, during the ice-free phase the lake circulation is weaker due to the lower wind speed, but is more variable due to the combined influences of thermal and wind forcing. The depth-averaged circulation features a pronounced mid-lake cyclonic gyre under the prevailing southwesterly wind and positive wind stress curl, but shows an anti-cyclonic gyre in the central-western lake when the southwesterly wind weakens or becomes intermittent, hence the effects of the positive wind stress curl overwhelm the effects of thermal structure. This strong dependence of the lake circulation to wind stress curl is consistent with previous findings by Beletsky et al. (2006, 2012, 2013) based on both observations and simulations in the southern Lake Michigan and central Lake Erie.

Presently, valuable observational data set for this large TP lake LNC is still insufficient due to its remoteness and harsh climatic conditions. Key observational data lacking includes the over-lake winds, multi-point water temperature profiles, and water currents. This limits the full evaluation of the present ICEPOM simulation results, and we expect that model improvement will be guided by further evaluation when more comprehensive observations of lake temperature and currents become available. Moreover, given the strong correspondence between the over-lake mesoscale pressure systems and lake circulation (Emery & Csanady, 1973; Petterssen & Calabrese, 1959), the accuracy of the modeled summer-autumn circulation depends on the realism of the spatial variability of over-lake winds (Bennington et al., 2010). Beletsky et al. (2013) showed that for Lake Erie, wind fields from the Global Environmental Multiscale regional forecast system of Canada, which well capture the over-lake mesoscale wind structures, yield better thermo-hydrodynamic modeling results compared to interpolated wind fields from limited station observations. Similar findings have been reported for Lake Superior (Chen et al., 2004; Xue et al., 2015) and Lake Ontario (Huang et al., 2010), all emphasizing the need for high-resolution atmospheric forcing, that can accurately represent the over-lake mesoscale wind variability, for reliable thermo-hydrodynamic modeling. In this regard, we stress the need to expand in situ meteorological station networks around the lake. This would support better assimilation of observational data into reanalysis or numerical models, thus providing improved over-lake mesoscale wind forcing for hydrodynamic simulations.

The present modeling study also has several additional limitations. First, the influence of runoff from the glacier/snow-melting on lake thermodynamics is important for these high-altitude lakes but is not included in the model. Glacier meltwater typically introduces cold inflows. Satellite observations have revealed that over the past two decades, glacier-fed lakes on the TP have shown slower warming rates than non-glacier-fed lakes, and some glacier-fed lakes above the 4,200 m altitude even exhibit cooling trends (Song et al., 2016; Wan et al., 2018; Zhang et al., 2014). The air warming rate over TP during 1980–2018 was more than twofold the global average during 1961–2015 (0.44°C·decade^{-1} vs. 0.14°C·decade^{-1}, Zhang, Yao, et al., 2020). This favors the accelerated melting of glaciers and perennial snow cover (Bolch, 2012; Yao et al., 2019), and the influence of cold-water input needs to be included to reduce the uncertainties in lake thermodynamic modeling. Second, accurately quantifying the surface runoff inputs is crucial for predicting the long-term lake water budgets. Both precipitation-induced and glacier-melt runoff have significant contributions to the rapid expansion of TP lakes (Tong et al., 2016). This is particularly relevant for Lake Nam Co, located at the northeastern corner of the Nyainqentanglha Range (~6,000 m altitude), which receives inflows from more than 60 tributaries during summer, with the largest originating from the southwestern Nyainqentanglha Range (Wang et al., 2019; Zhou et al., 2013). The lake has experienced notable expansion in area, rising water levels, and shrinking glacier coverage in its catchment (Lei et al., 2013; Wu et al., 2014; Zhu et al., 2010). These findings underscore the imperative to incorporate meltwater inputs in future modeling efforts, while also highlight the critical need for enhanced basin-scale hydrological monitoring to constrain these processes. Lastly, future studies should also consider the heat/water exchange and material transport processes between the deep water and bottom sediments. The lake thermo-hydrodynamic information from the results of the present and future improved models has broad implications to the study of lake biogeochemical processes, for example, the distribution and transport of nutrients/contaminants, water quality and primary productivity. For such studies including predicting the ecological response of TP lakes to the pronounced climatic change, coupling ICEPOM to an ecosystem model is needed.

Data Availability Statement

We acknowledge the use of the MATLAB 2021b and NCAR Command Language version 6.6.2 (http://dx.doi.org/10.5065/D6WD3XH5) to analyze model results and plot the figures.

Acknowledgments
This study is funded by the National Natural Science Foundation of China under Grants 42305015, 41975081, CAS "Light of West China" Program (E129030101), the basic research fund of CAMS (2023Y012), the research project of Jiangsu Meteorological Bureau (KQ202313), the Research Funds for the Frontiers Science Center for Critical Earth Material Cycling Nanjing University, the Fundamental Research Funds for the Central Universities (020914380103), the Jiangsu University "Blue Project" outstanding young teachers training object, the Jiangsu Collaborative Innovation Center for Climate Change. We are grateful to three anonymous reviewers for their constructive comments that guided the revision of the originally submitted manuscript.

References

Austin, J. A., & Colman, S. M. (2007). Lake Superior summer water temperatures are increasing more rapidly than regional air temperatures: A positive ice-albedo feedback. *Geophysical Research Letters*, *34*(6). https://doi.org/10.1029/2006GL029021

Bai, P., Wang, J., Chu, P., Hawley, N., Fujisaki-Manome, A., Kessler, J., et al. (2020). Modeling the ice-attenuated waves in the Great Lakes. *Ocean Dynamics*, *70*(7), 991–1003. https://doi.org/10.1007/s10236-020-01379-z

Bai, X. Z., Wang, J., Schwab, D. J., Yang, Y., Luo, L., Leshkevich, G. A., & Liu, S. (2013). Modeling 1993-2008 climatology of seasonal general circulation and thermal structure in the Great Lakes using FVCOM. *Ocean Modelling*, *65*, 40–63. https://doi.org/10.1016/j.ocemod.2013.02.003

Beletsky, D., Hawley, N., & Rao, Y. R. (2013). Modeling summer circulation and thermal structure of Lake Erie. *Journal of Geophysical Research*, *118*(11), 6238–6252. https://doi.org/10.1002/2013JC008854

Beletsky, D., Hawley, N., Rao, Y. R., Vanderploeg, H. A., Beletsky, R., Schwab, D. J., & Ruberg, S. A. (2012). Summer thermal structure and anticyclonic circulation of Lake Erie. *Geophysical Research Letters*, *39*(6). https://doi.org/10.1029/2012GL051002

Beletsky, D., Saylor, J. H., & Schwab, D. J. (1999). Mean circulation in the Great Lakes. *Journal of Great Lakes Research*, *25*(1), 78–93. https://doi.org/10.1016/S0380-1330(99)70718-5

Beletsky, D., Schwab, D., & McCormick, M. (2006). Modeling the 1998-2003 summer circulation and thermal structure in Lake Michigan. *Journal of Geophysical Research*, *111*(C10). https://doi.org/10.1029/2005JC003222

Beletsky, D., & Schwab, D. J. (2001). Modelling circulation and thermal structures in Lake Michigan: Annual cycle and interannual variability. *Journal of Geophysical Research*, *106*, 745–771. https://doi.org/10.1029/2000jc000691

Bennington, V., McKinley, G. A., Kimura, N., & Wu, C. H. (2010). General circulation of Lake Superior: Mean, variability, and trends from 1979 to 2006. *Journal of Geophysical Research*, *115*(C12). https://doi.org/10.1029/2010JC006261

Bennington, V., Notaro, M., & Holman, K. D. (2014). Improving climate sensitivity of deep lakes within a regional climate model and its impact on simulated climate. *Journal of Climate*, *27*(8), 2886–2911. https://doi.org/10.1175/JCLI-D-13-00110.1

Blokhina, N. S., & Selin, D. I. (2019). Spring thermal bar formation in a water reservoir with a complex bottom relief (for Lake Ladoga as an example). *Moscow University Physics Bulletin*, *74*(1), 58–63. https://doi.org/10.3103/S0027134919010065

Blumberg, A. F., & Mellor, G. L. (1987). A description of a three-dimensional coastal ocean circulation model, three-dimensional coastal ocean circulation model. *Three-Dimensional Ocean Models*, *4*, 1–16. https://doi.org/10.1029/CO004p0001

Bolch, T., Kulkarni, A., Kääb, A., Huggel, C., Paul, F., Cogley, J. G., et al. (2012). The state and fate of Himalayan glaciers. *Science*, *336*(6079), 310–314. https://doi.org/10.1126/science.1215828

Boyce, F. M., Donelan, M. A., Hamblin, P. F., Murthy, C. R., & Simons, T. J. (1989). Thermal structure and circulation in the great lakes. *Atmosphere-Ocean*, *27*(4), 607–642. https://doi.org/10.1080/07055900.1989.9649358

Cai, Y., Ke, C. Q., Li, X. G., Zhang, G. Q., Duan, Z., & Lee, H. (2019). Variations of lake ice phenology on the Tibetan Plateau from 2001 to 2017 based on MODIS data. *Journal of Geophysical Research*, *124*(2), 825–843. https://doi.org/10.1029/2018JD028993

Chen, C. S., Xu, Q. C., Ralph, E., Budd, J. W., & Lin, H. C. (2004). Response of Lake Superior to mesoscale wind forcing: A comparison between currents driven by QuikSCAT and buoy winds. *Journal of Geophysical Research*, *109*(C10), C10S02. https://doi.org/10.1029/2002JC001692

Chen, T. A., & Millero, F. J. (1986). Thermodynamic properties for natural waters covering only the limnological range. *Limnology & Oceanography*, *31*(3), 657–662. https://doi.org/10.4319/lo.1986.31.3.0657

Csanady, G. T. (1977). On the cyclonic mean circulation of large lakes. *Proceedings of the National Academy of Sciences*, *74*(6), 2204–2208. https://doi.org/10.1073/pnas.74.6.2204

Emery, K. O., & Csanady, G. T. (1973). Surface circulation of lakes and nearly land-locked seas. *Proceedings of the National Academy of Sciences of the United States of America*, *70*(1), 93–97. https://doi.org/10.1073/pnas.70.1.93

Fairall, C. W., Bradley, E. F., Grachev, A. A., & Edson, J. B. (2003). Bulk parameterization of air–sea fluxes: Updates and verification for the COARE algorithm. *Journal of Climate*, *16*, 571–591. https://doi.org/10.1175/1520-0442(2003)016<0571:BPOASF>2.0.CO;2

Fairall, C. W., Bradley, E. F., Rogers, D. P., Edson, J. B., & Young, G. S. (1996). Bulk parameterization of air-sea fluxes for tropical ocean-global atmosphere coupled-ocean atmosphere response experiment. *Journal of Geophysical Research*, *101*(C2), 3747–3764. https://doi.org/10.1029/95JC03205

Fujisaki, A., Fitzpatrick, L. E., Gronewold, A. D., Anderson, E. J., Lofgren, B. M., Spence, C., et al. (2017). Turbulent heat fluxes during an extreme lake-effect snow event. *Journal of Hydrology*, *18*, 3145–3163. https://doi.org/10.1175/JHM-D-17-0062.1

Fujisaki, A., Wang, J., Bai, X. Z., Leshkevich, G., & Lofgren, B. (2013). Model-simulated interannual variability of Lake Erie ice cover, circulation, and thermal structure in response to atmospheric forcing, 2003-2012. *Journal of Geophysical Research*, *118*(9), 4286–4304. https://doi.org/10.1002/jgrc.20312

Fujisaki, A., Wang, J., Hu, H. G., Schwab, D. J., Hawley, N., & Rao, Y. R. (2012). A modeling study of ice–water processes for Lake Erie applying coupled ice-circulation models. *Journal of Great Lakes Research*, *38*(4), 585–599. https://doi.org/10.1016/j.jglr.2012.09.021

Gill, A. (1982). *Atmosphere-Ocean dynamics*. Academic.

Gou, P., Ye, Q. H., Che, T., Fang, Q., Ding, B. H., Lin, C. H., & Zong, J. B. (2017). Lake ice phenology of Nam Co, Central Tibetan Plateau, China, derived from multiple MODIS data products. *Journal of Great Lakes Research*, *43*(6), 989–998. https://doi.org/10.1016/j.jglr.2017.08.011

Guo, L. N., Wu, Y. H., Zheng, H. X., Zhang, B., Li, J. S., Zhang, F. S., & Shen, Q. (2018). Uncertainty and variation of remotely sensed lake ice phenology across the Tibetan Plateau. *Remote Sensing*, *10*, 1534. https://doi.org/10.3390/rs10101534

Harrington, M. W. (1895). *Surface currents of the great Lakes: As deduced from the movements of bottle papers during the seasons of 1892, 1893, and 1894*. Bulletin/U.S. Department of Agriculture.

He, J., Yang, K., Tang, W. J., Lu, H., Qin, J., Chen, Y. Y., & Li, X. (2020). Data Descriptor: The first high-resolution meteorological forcing dataset for land process studies over China [Dataset]. *Scientific Data*, *7*(25), 1–11. https://doi.org/10.1038/s41597-020-0369-y

Hibler, W. D. (1979). A dynamic thermodynamic sea ice model. *Journal of Physical Oceanography*, *9*(4), 815–846. https://doi.org/10.1175/1520-0485(1979)009<0815:ADTSIM>2.0.CO;2

Hibler, W. D. (1980). Modeling a variable thickness sea ice cover. *Monthly Weather Review*, *108*(12), 1943–1973. https://doi.org/10.1175/1520-0493(1980)108<1943:MAVTSI>2.0.CO;2

Holland, P. R., & Kay, A. (2003). A review of the physics and ecological implications of the thermal bar circulation. *Limnologica*, *33*(3), 153–162. https://doi.org/10.1016/S0075-9511(03)80011-7

Hsu, S. A. (1988). *Coastal meteorology*. Academic Press Inc.

Huang, A. N., Rao, Y. R., & Lu, Y. Y. (2010). Evaluation of a 3-D hydrodynamic model and atmospheric forecast forcing using observations in Lake Ontario. *Journal of Geophysical Research*, *115*(C2), C02004. https://doi.org/10.1029/2009JC005601

Huang, L., Timmermann, A., Lee, S. S., Rodgers, K. B., Yamaguchi, R., & Chung, E. S. (2022). Emerging unprecedented lake ice loss in climate change projections. *Nature Communications*, *13*(1), 5798. https://doi.org/10.1038/s41467-022-33495-3

Huang, W. F., Zhang, J. R., Leppäranta, M., Li, Z. H., Cheng, B., & Lin, Z. J. (2019). Thermal structure and water-ice heat transfer in a shallow ice-covered thermokarst lake in central Qinghai-Tibet Plateau. *Journal of Hydrology*, *578*, 124122. https://doi.org/10.1016/j.jhydrol.2019.124122

Huang, W. F., Zhao, W., Zhang, C., Leppäranta, M., Li, Z. H., Li, R., & Lin, Z. J. (2021). Radiative penetration dominates the thermal regime and energetics of a shallow ice-covered lake in an arid climate. *The Cryosphere*. https://doi.org/10.5194/tc-2021-349

Hunke, E. C., & Dukowicz, J. K. (1997). An elastic-viscous-plastic model for sea ice dynamics. *Journal of Physical Oceanography*, *27*(9), 1849–1867. https://doi.org/10.1175/1520-0485(1997)027<1849:AEVPMF>2.0.CO;2

Ke, L. H., & Song, C. Q. (2014). Remotely sensed surface temperature variation of an inland saline lake over the central Qinghai–Tibet Plateau. *ISPRS J. Photogramm.*, *98*, 157–167. https://doi.org/10.1016/j.isprsjprs.2014.09.007

Kirillin, G., Shatwall, T., & Wen, L. J. (2021). Ice-covered lakes on Tibetan Plateau as solar heat collectors. *Geophysical Research Letters*, *48*(14). https://doi.org/10.1029/2021GL093429

Kirillin, G., Wen, L. J., & Shatwell, T. (2017). Seasonal thermal regime and climatic trends in lakes of the Tibetan highlands. *Hydrology and Earth System Sciences*, *21*(4), 1895–1909. https://doi.org/10.5194/hess-21-1895-2017

Kraemaer, B. M., Pilla, R. M., Woolway, R. I., Anneville, O., Ban, S., Colom-Montero, W., et al. (2021). Climate change drives widespread shifts in lake thermal habitat. *Nature Climate Change*, *11*(6), 521–529. https://doi.org/10.1038/s41558-021-01060-3

Lang, J. H., Lyu, S. H., Li, Z. G., Ma, Y. M., & Su, D. S. (2018). An investigation of ice surface albedo and its influence on the high-altitude lakes of the Tibetan Plateau. *Remote Sensing*, *10*(2), 218. https://doi.org/10.3390/rs10020218

Lazhu, Yang, K., Hou, J. Z., Wang, J. B., Lei, Y. B., Zhu, L. P., et al. (2020). A new finding on the prevalence of rapid water warming during lake ice melting on the Tibetan Plateau. *Scientific Bulletin*, *66*(23), 2358–2361. https://doi.org/10.1016/j.scib.2021.07.022

Lei, Y. B., Yao, T. D., Bird, B. W., Yang, K., Zhai, J. Q., & Sheng, Y. W. (2013). Coherent lake growth on the central Tibetan Plateau since the 1970s: Characterization and attribution. *Journal of Hydrology*, *483*, 61–67. https://doi.org/10.1016/j.jhydrol.2013.01.003

Li, X. Y., Peng, S. S., Xi, Y., Woolway, R. I., & Liu, G. (2022). Earlier ice loss accelerates lake warming in the Northern Hemisphere. *Nature Communications*, *13*(1), 5156. https://doi.org/10.1038/s41467-022-32830-y

Lu, S. L., Ma, J., Ma, X. Q., Tang, H. L., Zhao, H. L., & Baig, M. H. A. (2019). Time series of the inland surface water dataset in China (ISWDC) for 2000-2016 derived from MODIS archives. *Earth System Science Data*, *11*(3), 1099–1108. https://doi.org/10.5194/essd-11-1099-2019

Maberly, S. C., O'Donnell, R. A., Woolway, R. I., Cutler, M. E. J., Gong, M. Y., Jones, I. D., et al. (2020). Global lake thermal regions shift under climate change. *Nature Communications*, *11*(1), 1232. https://doi.org/10.1038/s41467-020-15108-z

McCULLOCH, J. A. W. (1973). The international field year for the great lakes. *Hydrological Sciences Journal*, *18*(3), 367–373. https://doi.org/10.1080/02626667309494047

Mellor, G. L., & Yamada, T. (1982). Development of a turbulence closure model for geophysical fluid problems. *Reviews of Geophysics and Space Physics*, *20*(4), 851–875. https://doi.org/10.1029/RG020i004p00851

Monismith, S. G., Imberger, J., & Morison, M. L. (1990). Convective motions in the sidearm of a small reservoir. *Limnology & Oceanography*, *35*(8), 1676–1702. https://doi.org/10.4319/lo.1990.35.8.1676

Mortimer, C. H. (1987). Fifty years of physical investigations and related limnological studies on Lake Erie, 1928-1977. *Journal of Great Lakes Research*, *13*(4), 407–435. https://doi.org/10.1016/S0380-1330(87)71664-5

Muñoz-Sabater, J. (2019). ERA5-Land hourly data from 1981 to present [Dataset]. *Copernicus Climate Change Service (C3S) Climate Data Store (CDS)*. https://doi.org/10.24381/cds.e2161bac

Parkinson, C. L., & Washington, W. M. (1979). A large-scale numerical model of sea ice. *Journal of Geophysical Research*, *84*(C1), 311–337. https://doi.org/10.1029/JC084iC01p00311

Petterssen, S., & Calabrese, P. A. (1959). On some weather influence due to warming of the air by the great lakes in winter. *Journal of the Atmospheric Sciences*, *16*(6), 646–652. https://doi.org/10.1175/1520-0469(1959)016<0646:OSWIDT>2.0.CO;2

Pickett, R. L., & Richards, P. F. (1975). Lake Ontario mean temperatures and currents in July, 1972. *Journal of Physical Oceanography*, *5*(4), 775–781. https://doi.org/10.1175/1520-0485(1975)005<0775:LOMTAC>2.0.CO;2

Pilla, R. M., & Williamson, C. E. (2021). Earlier ice breakup induces changepoint responses in duration and variability of spring mixing and summer stratification in dimictic lakes. *Limnology and Oceanography*, *67*(S1), S173–S183. https://doi.org/10.1002/lno.11888

Qi, M. M., Liu, S. Y., Yao, X. J., Xie, F. M., & Gao, Y. P. (2020). Monitoring the ice phenology of Qinghai Lake from 1980 to 2018 using multisource remote sensing data and google earth engine. *Remote Sensing*, *12*(14), 2217. https://doi.org/10.3390/rs12142217

Qi, M. M., Yao, X. J., Li, X. F., Duan, H. Y., Gao, Y. P., & Liu, J. (2019). Spatiotemporal characteristics of Qinghai Lake ice phenology between 2000 and 2016. *Journal of Geographical Sciences*, *29*(1), 115–130. https://doi.org/10.1007/s11442-019-1587-0

Qi, S., & Xue, P. F. (2019). Impact of lake surface temperature variations on lake effect snow cover over the Great Lakes region. *Journal of Geophysical Research*, *124*. https://doi.org/10.1029/2019JD031261

Qiu, J. (2008). China: The third pole. *Nature*, *454*(7203), 393–396. https://doi.org/10.1038/454393a

Qu, B., Kang, S. C., Chen, F., Zhang, Y. J., & Zhang, G. S. (2012). Lake ice and its effect factors in the Nam Co basin, Tibetan Plateau (in Chinese). *Progressus Inquisitiones De Mutatione Climatis*, *8*(5), 327–333. https://doi.org/10.3969/j.issn.1673-1719.2012.05.003

Rao, Y. R., Skafel, M. G., & Charlton, M. N. (2004). Circulation and turbulent exchange characteristics during the thermal bar in Lake Ontario. *Limnology & Oceanography*, *49*(6), 2190–2200. https://doi.org/10.4319/lo.2004.49.6.2190

Schwab, D. J., & Beletsky, D. (2003). Relative effects of wind stress curl, topography, and stratification on large-scale circulation in Lake Michigan. *Journal of Geophysical Research*, *108*(C2), 3044. https://doi.org/10.1029/2001JC001066

Schwab, D. J., O'Connor, W. P., & Mellor, G. L. (1995). On the net cyclonic circulation in large stratified lakes. *Journal of Physical Oceanography*, *25*(6), 1516–1520. https://doi.org/10.1175/1520-0485(1995)025<1516:OTNCCI>2.0.CO;2

Semtner, A. J. (1976). A model for the thermodynamic growth of sea ice in numerical investigations of climate. *Journal of Physical Oceanography*, *6*(3), 379–389. https://doi.org/10.1175/1520-0485(1976)006<0379:AMFTTG>2.0.CO;2

Smagorinsky, J. (1963). General circulation experiments with the primitive equation. I. The basic experiment. *Monthly Weather Review*, *21*, 99–165. https://doi.org/10.1175/1520-0493(1963)091<0099:GCEWTP>2.3.CO;2

Song, K. S., Wang, M., Du, J., Yuan, Y., Ma, J. H., Wang, M., & Mu, G. Y. (2016). Spatiotemporal variations of lake surface temperature across the Tibetan Plateau using MODIS LST product. *Remote Sensing*, *8*(10), 854. https://doi.org/10.3390/rs8100854

Su, R. M. Z., Ma, W. Q., Ma, Y. M., Xie, Z. P., Wang, B. B., Hu, W., et al. (2021). Investigation of thermal stratification and mixed layer depth in La'ang Co in the Tibetan Plateau (in Chinese). *Journal of Lake Sciences*, *33*(2), 550–560. https://doi.org/10.18307/2021.0220

Subin, Z. M., Riley, W. J., & Mironov, D. (2012). An improved lake model for climate simulations: Model structure, evaluation, and sensitivity analyses in CESM1. *Journal of Advances in Modeling Earth Systems*, *4*(1), M02001. https://doi.org/10.1029/2011MS000072

Sun, X., Xie, L., Semazzi, F. H. M., & Liu, B. (2014). A numerical investigation of the precipitation over Lake Victoria basin using a coupled atmosphere-lake limited-area model. *Advances in Meteorology*, *2014*, 1–15. https://doi.org/10.1155/2014/960924

Tikhomirov, A. I. (1963). The thermal bar of Lake Ladoga. *Bull. (Izvestia) All-Union Geogr. Soc.*, *95*, 134–142.

Titze, D. J., & Austin, J. A. (2014). Winter thermal structure of Lake Superior. *Limnology & Oceanography*, *59*(4), 1336–1348. https://doi.org/10.4319/lo.2014.59.4.1336

Toffolon, M., Piccolroaz, S., Majone, B., Soja, A. M., Peeters, F., Schmid, M., & Wüest, A. (2014). Prediction of surface temperature in lakes with different morphology using air temperature. *Limnology & Oceanography*, *59*(6), 2185–2202. https://doi.org/10.4319/lo.2014.59.6.2185

Tong, K., Su, F. G., & Xu, B. Q. (2016). Quantifying the contribution of glacier meltwater in the expansion of the largest lake in Tibet. *Journal of Geophysical Research*, *121*(19), 11158–11173. https://doi.org/10.1002/2016JD025424

Tsydenov, B. O. (2019). A numerical study of the thermal bar in shallow water during the autumn cooling. *Journal of Great Lakes Research*, *45*(4), 715–725. https://doi.org/10.1016/j.jglr.2019.05.012

Wan, W., Zhao, L., Xie, H., Liu, B., Li, H., Cui, Y., et al. (2018). Lake surface water temperature change over the Tibetan plateau from 2001 to 2015: A sensitive indicator of the warming climate. *Geophysical Research Letters*, *45*(11), 177–186. https://doi.org/10.1029/2018GL078601

Wang, B. B., Ma, Y. M., Chen, X. L., Ma, W. Q., Su, Z. B., & Menenti, M. (2015). Observation and simulation of lake-air heat and water transfer process in a high-latitude shallow lake on the Tibetan Plateau. *Journal of Geophysical Research*, *120*(24), 12327–12344. https://doi.org/10.1002/2015JD023863

Wang, J., Bai, X. Z., Hu, H. G., Clites, A., Colton, M., & Lofgren, B. (2012). Temporal and spatial variability of Great Lakes ice cover, 1973-2010. *Journal of Climate*, *25*(4), 1318–1329. https://doi.org/10.1175/2011JCLI4066.1

Wang, J. B. (2020). Water temperature observation data at Nam Co Lake in Tibet (2011-2014). *National Tibetan Plateau Data Center*. https://doi.org/10.11888/Hydro.tpdc.270332

Wang, J. B., Huang, L., Ju, J. T., Daut, G., Ma, Q. F., Zhu, L. P., et al. (2020). Seasonal stratification of a deep, high-altitude, dimictic lake: Nam Co, Tibetan Plateau. *Journal of Hydrology*, *584*, 124668. https://doi.org/10.1016/j.jhydrol.2020.124668

Wang, J. B., Huang, L., Ju, J. T., Daut, G., Wang, Y., Ma, Q. F., et al. (2019). Spatial and temporal variations in water temperature in a high-altitude deep dimictic mountain lake (Nam Co), central Tibetan Plateau. *Journal of Great Lakes Research*, *45*(2), 212–223. https://doi.org/10.1016/j.jglr.2018.12.005

Wang, J. B., Ping, P., Ma, Q. F., & Zhu, L. P. (2013). Investigation of water depth, water quality and modern sedimentation rate in Mapam Yumco and La'ang Co, Tibet (in Chinese). *Journal of Lake Sciences*, *25*, 609–616. https://doi.org/10.18307/2013.0420

Wang, J. B., Zhu, L. P., Daut, G., Ju, J. T., Lin, X., Wang, Y., & Zhen, X. L. (2009). Investigation of bathymetry and water quality of Lake Nam Co, the largest lake on the central Tibetan Plateau. *Limnology*, *10*(2), 149–158. https://doi.org/10.1007/s10201-009-0266-8

Wang, M. D., Hou, J. Z., & Lei, Y. B. (2014). Classification of Tibetan lakes based on variations in seasonal lake water temperature. *Chinese Science Bulletin*, *59*(34), 4847–4855. https://doi.org/10.1007/s11434-014-0588-8

Wetzel, R. G., & Likens, G. E. (2000). The heat budget of lakes. In *Limnological analyses*. Springer. https://doi.org/10.1007/978-1-4757-3250-4_4

Weyhenmeyer, G. A., Westöö, A. K., & Willén, E. (2007). Increasingly ice-free winters and their effects on water quality in Sweden's largest lakes. In *European Large Lakes Ecosystem changes and their ecological and socioeconomic impacts* (pp. 111–118). Springer.

Woolway, R. I., Kraemer, B. M., Lenters, J. D., Merchant, C. J., O'Reilly, C. M., & Sharma, S. (2020). Global lake responses to climate change. *Nature Reviews Earth & Environment*, *1*(8), 388–403. https://doi.org/10.1038/s43017-020-0067-5

Wright, D. M., Posselt, D. J., & Steiner, A. L. (2013). Sensitivity of lake-effect snowfall to lake ice cover and temperature in the Great Lakes region. *Monthly Weather Review*, *141*(2), 670–689. https://doi.org/10.1175/MWR-D-12-00038.1

Wu, Y., Huang, A. N., Fujisaki-Manome, A., Zhang, Z. Q., Dai, X. L., & Wang, Y. (2023). Application of a three-dimensional coupled hydrodynamic-ice model to assess spatiotemporal variations in ice cover and underlying mechanisms in Lake Nam Co, Tibetan Plateau, 2007-2017. *Journal of Geophysical Research*, *128*(24). https://doi.org/10.1029/2023JD038844

Wu, Y., Huang, A. N., Lazhu, Yang, X. Y., Qiu, B., Wen, L. J., et al. (2020). Improvements of the coupled WRF-Lake model over Lake Nam Co, Central Tibetan Plateau. *Climate Dynamics*, *55*(9–10), 2703–2724. https://doi.org/10.1007/s00382-020-05402-3

Wu, Y., Huang, A. N., Li, X., Wen, L. J., Li, J., & Li, J. Y. (2024). Thermal response of large seasonally ice-covered lakes over Tibetan Plateau to climate change. *Journal of Geophysical Research*, *129*(8). https://doi.org/10.1029/2023JD039935

Wu, Y., Huang, A. N., Lu, Y. Y., Lazhu, Yang, X. Y., Qiu, B., et al. (2021). Numerical study of the thermal structure and circulation in a large and deep dimictic lake over Tibetan Plateau. *Journal of Geophysical Research*, *126*(10). https://doi.org/10.1029/2021JC017517

Wu, Y. H., Zheng, H. X., Zhang, B., Chen, D. L., & Lei, L. P. (2014). Long-term changes of lake level and water budget in the Nam Co Basin, central Tibetan Plateau. *Journal of Hydrometeorology*, *15*(3), 1312–1322. https://doi.org/10.1175/JHM-D-13-093.1

Wunsch, C. (1973). On the mean drift in large lakes. Limnol. *Oceanor*, *18*(5), 793–794. https://doi.org/10.4319/lo.1973.18.5.0793

Xiao, F., Ling, F., Du, Y., Feng, Q., Yan, Y., & Chen, H. (2013). Evaluation of spatial-temporal dynamics in surface water temperature of Qinghai Lake from 2001 to 2010 by using MODIS data. *Journal of Arid Land*, *5*(4), 452–464. https://doi.org/10.1007/s40333-013-0188-5

Xiao, Y., Xie, S. Y., Wang, M. D., He, Y., & Hou, J. Z. (2015). Characteristics of water temperature based on fractal and R/S method in Bangong Co and Dagze Co (in Chinese). *Geological Science and Technology Information*, *34*, 200–206.

Xue, P. F., Pal, J. S., Ye, X. Y., Lenters, J. D., Huang, C. F., & Chu, P. Y. (2017). Improving the simulation of large lakes in regional climate modeling: Two-way lake-atmosphere coupling with a 3D hydrodynamic model of the Great Lakes. *Journal of Climate*, *30*(5), 1605–1627. https://doi.org/10.1175/JCLI-D-16-0225.1

Xue, P. F., Schwab, D. J., & Hu, S. (2015). An investigation of the thermal response to meteorological forcing in a hydrodynamic model of Lake Superior. *Journal of Geophysical Research: Oceans*, *120*(7), 5233–5253. https://doi.org/10.1002/2015JC010740

Yao, T. D., Xue, Y. K., Chen, D. L., Chen, F. H., Thompson, L., Cui, P., et al. (2019). Recent Third Pole's Rapid warming accompanies cryospheric melt and water cycle intensification and interactions between monsoon and environment: Multidisciplinary approach with observations, modeling, and analysis. *Bulletin America Meteorology Society*, *100*(3), 423–444. https://doi.org/10.1175/BAMS-D-17-0057.1

Zhang, G. Q., Chen, W. F., Zheng, G. X., Xie, H. J., & Shum, C. K. (2020). Are China's water bodies (lakes) underestimated? *Proceedings of the National Academy of Sciences*, *117*(12), 6308–6309. https://doi.org/10.1073/pnas.192250117

Zhang, G. Q., Yao, T. D., Xie, H. J., Qin, J., Ye, Q. H., Dai, Y. F., & Guo, R. F. (2014). Estimating surface temperature changes of lakes in the Tibetan Plateau using MODIS LST data. *Journal of Geophysical Research: Atmospheres*, *119*(14), 8552–8567. https://doi.org/10.1002/2014JD021615

Zhang, G. Q., Yao, T. D., Xie, H. J., Yang, K., Zhu, L. P., Shum, C. K., et al. (2020). Response of Tibetan Plateau lakes to climate change: Trends, patterns, and mechanisms. *Earth-Science Reviews*, *208*, 103269. https://doi.org/10.1016/j.earscirev.2020.103269

Zhong, Y. F., Notaro, M., Vavrus, S. J., & Foster, M. J. (2016). Recent accelerated warming of the Laurentian Great Lakes: Physical drivers. *Limnology & Oceanography*, *61*(5), 1762–1786. https://doi.org/10.1002/lno.10331

Zhou, S. Q., Kang, S. C., Chen, F., & Joswiak, D. R. (2013). Water balance observations reveal significant subsurface water seepage from Lake Nam Co, south-central Tibetan Plateau. *Journal of Hydrology*, *491*, 89–99. https://doi.org/10.1016/j.jhydrol.2013.03.030

Zhu, L. P., Xie, M. P., & Wu, Y. H. (2010). Quantitative analysis of lake area variations and the influence factors from 1971 to 2004 in the Nam Co Basin of the Tibetan Plateau. *Chinese Science Bulletin*, *55*(13), 1294–1303. https://doi.org/10.1007/s11434-010-0015-8